Martín-Solís, J.R., Loarte, A., Lehnen, M. (2017). Formation and termination of runaway beams in ITER disruptions. *Nuclear Fusion*, 57(6), 066025, [28] p.

DOI: https://doi.org/10.1088/1741-4326/aa6939

Formation and termination of runaway beams in ITER disruptions

J.R. Martín-Solís[1,a], **A. Loarte**[2] **and M. Lehnen**[2]

[1] Universidad Carlos III de Madrid, Avenida de la Universidad 30, 28911-Madrid, Spain
[2] ITER Organization, Route de Vinon sur Verdon, CS 90046, 13067 St Paul Lez Durance Cedex, France

E-mail: solis@fis.uc3m.es

Abstract

A self-consistent analysis of the relevant physics regarding the formation and termination of runaway beams during mitigated disruptions by Ar and Ne injection is presented for selected ITER scenarios with the aim of improving our understanding of the physics underlying the runaway heat loads onto the plasma facing components (PFCs) and identifying open issues for developing and accessing disruption mitigation schemes for ITER. This is carried out by means of simplified models, but still retaining sufficient details of the key physical processes, including: (a) the expected dominant runaway generation mechanisms (avalanche and primary runaway seeds: Dreicer and hot tail runaway generation, tritium decay and Compton scattering of γ rays emitted by the activated wall), (b) effects associated with the plasma and runaway current density profile shape, and (c) corrections to the runaway dynamics to account for the collisions of the runaways with the partially stripped impurity ions, which are found to have strong effects leading to low runaway current generation and low energy conversion during current termination for mitigated disruptions by noble gas injection (particularly for Ne injection) for the shortest current quench times compatible with acceptable forces on the ITER vessel and in-vessel components ($\tau_{res} \sim 22$ ms). For the case of long current quench times ($\tau_{res} \sim 66$ ms), runaway beams up to $\sim$10 MA can be generated during the disruption current quench and, if the termination of the runaway current is slow enough, the generation of runaways by the avalanche mechanism can play an important role, increasing substantially the energy deposited by the runaways onto the PFCs up to a few hundreds of MJs. Mixed impurity (Ar or Ne) plus deuterium injection proves to be effective in controlling the formation of the runaway current during the current quench, even for the longest current quench times, as well as in decreasing the energy deposited on the runaway electrons during current termination.

Keywords: disruption, runaway electrons, runaway seed, runaway avalanche, ITER

1. Introduction

Large runaway (RE) currents are expected to be formed during the current quench (CQ) phase of disruptions in ITER [1]. There is large concern about these energetic electrons as they can cause melting when they impact on the plasma facing components (PFCs) [2]. Runaway electrons usually deposit their energy in very short pulses and on localized areas of the plasma facing components leading to a reduction of their lifetime and, in some cases, requiring their replacement.

Although the main interest of studying runaway plasmas is related to their final deposition, most of the runaway electron studies during disruptions have been devoted to the generation of the runaway current during the disruption current quench. However, during the termination phase of the disruption, when the plasma current and the runaway electrons are lost, conversion of the magnetic energy of the runaway plasma into runaway kinetic energy can occur. This can increase substantially the energy fluxes deposited by the runaway electrons on the

[a] This work was carried out with financial support from the ITER Organization under contract IO/13/CT/430000875.

PFCs in comparison with the values expected from the runaway kinetic energy gain during the disruption current quench. Conversion of magnetic into runaway kinetic energy during termination was first proposed in [3], and experimental evidence reported in JET and DIII-D [4, 5]. In [6], an inter-machine comparison was presented for the termination phase of disruptions with runaway current plateau formation for three devices (JET, DIII-D and FTU) with substantially different plasma currents and sizes which, together with simple 0D modelling, allowed the identification of the dominant physical processes determining the conversion of magnetic into runaway kinetic energy during disruption termination. The efficiency of conversion of the magnetic energy of the plateau runaway plasma into runaway kinetic energy during the disruption termination phase was found to be larger for slow terminations (i.e. long duration of the runaway loss) and to decrease when the resistive time of the residual ohmic plasma after the disruption current quench increases [6]. Secondary runaway generation by avalanche during runaway terminations also leads to an increase in the conversion of magnetic energy into runaway kinetic energy but this is only sizeable for high runaway currents and for long durations of the termination. In addition, penetration of the magnetic energy external to the vacuum vessel has to be taken into account when the timescale of the runaway termination is longer than the vacuum vessel resistive time.

In this paper, an analysis of the runaway generation and termination for selected ITER disruption scenarios is addressed, in which the results of the modelling of the disruption current quench and runaway current formation provides the basic inputs for the termination phase of the runaway plasma and runaway power deposition on the PFCs. The aim of the work is to improve our understanding of the physics underlying the runaway heat loads onto the PFCs in ITER disruptions which will be done by means of simplified models, but still retaining the essentials of the involved physical processes, and applied to a range of ITER scenarios, providing an initial assessment which should help to identify the most relevant issues for a more detailed modelling. Mitigated disruptions by both Ar and Ne injection are considered. The effect of the expected dominant runaway generation mechanisms, including runaway avalanche and the runaway primary seeds (Dreicer, hot tail runaway generation, tritium decay and Compton scattering of γ-rays emitted by the wall) is taken into account. In addition, a proper treatment of the runaway dynamics in plasmas with high impurity content, which takes into account the collisions with the free and bound electrons and the scattering by the full nuclear and the electron-shielded ion charge, and of the effects associated with the plasma and runaway current density profile evolution are also included. The basic model equations for the current density profile evolution, runaway generation mechanisms and impurity effects on the runaway dynamics are presented in section 2. The formation the runaway beam (runaway current and kinetic beam energy) and the conversion of magnetic into runaway kinetic energy during termination of the resulting runaway current are discussed in section 3.1 and 3.2, respectively. These provide the estimates of the total energy deposited by the runaway electrons during the termination phase of the disruption. The effectiveness of mixed Ar + D or Ne + D injection in decreasing the energy deposited by the runaways on the PFCs for the potentially most pessimistic disruption scenarios is analyzed in section 3.3. Finally, the conclusions are summarized in section 4 and open issues for a more accurate modelling and the development of disruption mitigation schemes for ITER are identified.

2. The disruption model

2.1. Basic equations

A one-dimensional (1D) model, taking into account the evolution of the plasma and runaway current density profiles during the disruption, has been developed. Although a zero dimensional analysis of the current quench and termination phase of the disruption is appropiate to identify many of the essential processes and parameters determining the formation of the runaway current as well as the conversion of magnetic into kinetic energy of the runaway electrons during current termination [6–9], there is evidence indicating that current profile shape effects might be important for both the formation and termination of the runaway beam during disruptions. For example, soft x-ray observations [10] and estimates of the plasma internal inductance [4], $l_{\rm int}$, through the current quench of JET disruptions support a peaking of the current density profile during the formation of the runaway beam, in agreement with theoretical predictions based on self-consistent modeling of the plasma and runaway current density profiles during the disruption [11, 12]. This might have important implications for ITER as: (1) due to the increase in the plasma internal inductance, at the same current, the magnetic energy of the runaway plasma would be substantially larger; (2) the post-current quench plasma current might become MHD unstable, as plasmas with steep current profiles can be prone to the tearing-mode instability [13, 14].

Our model is similar to others previously used to simulate the behavior of runaway discharges in various tokamaks, including both the CQ phase [12, 15] and the runaway current termination phase of the disruption [4]. It uses a simple plasma geometry, a straight, circular cylinder ($r < a$) surrounded by a thin conducting wall with a finite resistivity. The evolution of the plasma current density ($j_{\rm p}$) is evaluated by solving the current diffusion equation in a plasma with a runaway component,

$$\mu_0 \frac{\partial j_{\rm p}}{\partial t} = \nabla^2 E_{\|}, \qquad (1)$$

which, using cylindrical coordinates, and $E_{\|} = \eta\,(j_{\rm p} - j_{\rm r})$ ($j_{\rm p,r}$ are the plasma and runaway current densities, respectively), can be written as

$$\mu_0 \frac{\partial j_{\rm p}}{\partial t} = \frac{1}{r}\frac{\partial}{\partial r}\left[r\frac{\partial E_{\|}}{\partial r}\right] = \frac{1}{r}\frac{\partial}{\partial r}\left[r\frac{\partial \eta (j_{\rm p} - j_{\rm r})}{\partial r}\right]. \qquad (2)$$

The current produced by the runaway electrons is determined by a simple model including the seed due to the primary generation mechanisms and the secondary (avalanche) generation process, as well as runaway losses described by a characteristic runaway loss time, $\tau_{\rm L}$,

$$\frac{\partial j_r}{\partial t} = \left(\frac{\partial j_r}{\partial t}\right)_{seed} + \left(\frac{\partial j_r}{\partial t}\right)_{avalanche} - \frac{j_r}{\tau_L}. \quad (3)$$

The primary generation mechanisms will be discussed in section 2.3 and include the Dreicer [16, 17] and hot tail runaway electron generation mechanisms [18], but also tritium decay and Compton scattering of γ rays emitted by the activated wall during DT operation in ITER. The avalanche generation process is estimated as

$$\left(\frac{\partial j_r}{\partial t}\right)_{avalanche} \approx \frac{j_r}{\tau_s}, \quad (4)$$

where τ_s is the characteristic avalanching time which will be approximated by [3],

$$\tau_s \approx \frac{4\pi\varepsilon_0^2 m_e^2 c^3}{e^4 n_e} a(Z_{eff}) \left(\frac{E_\parallel}{E_R} - 1\right)^{-1}, \quad (5)$$

with $a(Z_{eff}) \approx \sqrt{3\,(5+Z_{eff})/\pi}$ and E_R, the critical field for runaway generation [17, 19], given by

$$E_R = \frac{n_e e^3 \ln\Lambda}{4\pi\varepsilon_0^2 m_e c^2}. \quad (6)$$

This estimate of τ_s is based on the Rosenbluth–Putvinski approximation [19] which, nevertheless, as pointed out in [20, 21], can be subject to limitations, particularly during the early phases of the avalanche.

Typically, during the current quench, the avalanche multiplication of the initial runaway seed is found to lead to the formation of a runaway current plateau. However, for sufficiently large densities (and so E_R), the electric field can drop below E_R before the runaway plateau is formed. As a result, when the electric field equals E_R during the current quench, the runaway avalanche is stopped (equations (4) and (5)), and a runaway current plateau is not formed, i.e. the runaway current reaches a maximum and starts to decay. In [9], it was shown that the resulting runaway current decay when $E_\parallel < E_R$, due to the collisions of the runaway electrons with the plasma particles, could be described by

$$\frac{\partial j_r}{\partial t} \approx \frac{e\,(E_\parallel - E_R)\, j_r}{m_e c \ln\Lambda\, a(Z_{eff})}. \quad (7)$$

Regarding the runaway losses, other descriptions (instead of the characteristic loss time, τ_L) might be used, such as a radial diffusion term, $\frac{1}{r}\frac{\partial}{\partial r} r\, D\, \frac{\partial j_r}{\partial r}$ (where D would be the runaway radial diffusion coefficient). Nevertheless, taking into account the uncertainties regarding the processes leading to the final loss of the runaway plasma, the description of the runaway losses in equation (3) in terms of a characteristic loss time, τ_L, turns out to be simple and adequate at a first stage for a direct comparison with 0D results [6]. As it will be discussed in section 3.2, non-uniform radial losses, $\tau_L(r)$, can be also assumed.

Effects associated with the induced currents in the vessel and the penetration of external magnetic energy can also be considered imposing an electric field at the edge, $E_\parallel \approx I_v R_v / 2\pi R_0$, where the vessel current, I_v, can be derived from

$$\frac{d}{dt}(M\, I_p + L_v\, I_v) \approx -I_v\, R_v. \quad (8)$$

Here M and L_v are the mutual plasma—vessel inductance and the vessel inductance, respectively, $M \approx L_v$, and R_v is the vessel resistance, which determines the vessel resistive time, $\tau_v \equiv L_v/R_v$. The ITER vacuum vessel has very low resistivity, which leads to very long timescales for the penetration of the external magnetic energy through it ($\tau_v \approx 500$ ms). This time is much larger than the expected current quench times in ITER, so that the effect of penetration of external magnetic energy during the disruption CQ is small. This has been quantitatively demonstrated by 0D calculations [38] and, therefore, for simplicity, this effect will not be included in our ITER study with the 1D model presented here.

2.2. Impurity effects

For plasmas with high impurity content, as those expected during the injection of noble gases for disruption mitigation purposes, corrections to the runaway dynamics must be considered to account for the collisions of the relativistic runaway electrons with the partially stripped impurity ions, including the effect of the collisions with free and bound electrons, as well as the scattering by the full nuclear and the electron-shielded ion charge, which should be described by the proper Coulomb logarithms [22, 23].

A detailed analysis carried out in [23] has shown that, under these conditions, the runaway dynamics can be properly described by replacing, in the collision terms, the factor $n_e \ln\Lambda$ used in plasmas with low impurity content by a parameter describing the collisions of the runaway electrons with the free and bound electrons,

$$\alpha_e = n_{ef} \ln\Lambda_{ef} + n_{eb} \ln\Lambda_{eb}, \quad (9)$$

(where n_{ef} and n_{eb} are the free and bound electron densities and $\ln\Lambda_{ef}$, $\ln\Lambda_{eb}$ the Coulomb logarithms for the collisions with free and bound electrons [22], respectively), and Z_{eff} by the effective ion collision charge

$$Z_{coll} = \frac{n_H \ln\Lambda_{eH} + \sum_j n_{z\,j}(< Z >_j^2 \ln\Lambda_{e<Z>_j} + Z_{0,j}^2 \ln\Lambda_{eZ_{0j}})}{n_{ef}\ln\Lambda_{ef} + n_{eb}\ln\Lambda_{eb}}, \quad (10)$$

which includes the effect of the collisions with the full nuclear and the electron-shielded ion charge of the impurity ions. The sum is over all the impurities species, where n_{zj}, $<Z>_j$ and $Z_{0,j}$ are the density, the average charge state and the full nuclear charge of the impurity j, respectively, and $\ln\Lambda_{eH}$, $\ln\Lambda_{e<Z>}$ and $\ln\Lambda_{eZ_0}$ are the Coulomb logarithms describing the collisions with the plasma protons (deuterium and tritium), the electron-bound-shielded impurities and with the full nuclear ion charge [22]. Both collisional coefficients, α_e and Z_{coll}, are not constant but depend on the electron energy as a result of the dependence of the Coulomb logarithms on the electron energy [22].

The collisions with the impurity ions increase the value of the critical field for runaway generation, which should include the effect of the collisions with the free and bound electrons [23],

$$E_{\rm R} \approx \frac{e^3\,\alpha_{\rm e}}{4\pi\varepsilon_0^2 m_{\rm e}c^2} = \frac{e^3\,(n_{\rm ef}\ln\Lambda_{\rm ef} + n_{\rm eb}\ln\Lambda_{\rm eb})}{4\pi\varepsilon_0^2 m_{\rm e}c^2}, \quad (11)$$

as well as modify the runaway growth rate associated with the avalanche mechanism and the primary runaway seeds.

Hence, following [23] (based on [24]), the growth rate of the secondary runaway electrons can be obtained by integrating the source rate of the secondaries knocked out of the background distribution, yielding

$$\frac{{\rm d}n_{\rm r}}{{\rm d}t} \approx \frac{2\pi r_{\rm e}^2 n_{\rm e} n_{\rm r}\, c}{(1+q_{\rm c}^2)^{1/2}-1}, \quad (12)$$

where $q_{\rm c}$ is the critical momentum (normalized to $m_{\rm e}c$) for runaway generation and $r_{\rm e}$ is the electron classical radius.

The effect of the collisions with the partially stripped impurities on the avalanche growth rate can be included considering that [23]: (1) both, free and bound electrons may become runaways (as the binding energy of the bound electrons for the impurities here considered (Ar and Ne) is much smaller than the MeV energies of the incident runaways), so that, $n_{\rm e}$ should be replaced by $n_{\rm e,tot} = n_{\rm ef} + n_{\rm eb}$; (2) the critical momentum for runaway generation, $q_{\rm c}$, is determined by the collisional dynamics of the runaway electrons which, in this case, should take into account the collisions with the free and bound electrons, as well as the scattering by the full nuclear and the electron-shielded ion charge ($\alpha_{\rm e}$ and $Z_{\rm coll}$ instead of $(n_{\rm e}\ln\Lambda)$ and $Z_{\rm eff}$, equations (9) and (10)). Thus, the avalanche runaway growth rate can be estimated [23]:

$$\left(\frac{{\rm d}j_{\rm r}}{{\rm d}t}\right)_{\rm avalanche} \approx \frac{e\,(E_\parallel - E_{\rm R})\,j_{\rm r}}{m_{\rm e}c\,\ln\Lambda\,a(Z_{\rm eff})} \;\rightarrow\; \left(\frac{{\rm d}j_{\rm r}}{{\rm d}t}\right)_{\rm avalanche} \approx \frac{e\,n_{\rm e,tot}\,(E_\parallel - E_{\rm R})\,j_{\rm r}}{m_{\rm e}c\,\alpha_{\rm e}(\gamma_{\rm c})\,a(Z_{\rm coll}(\gamma_{\rm c}))} \quad (13)$$

where $\alpha_{\rm e}$ and $Z_{\rm coll}$ must be evaluated at the critical energy for runaway generation, $\gamma_{\rm c}$ [23] (γ is the relativistic gamma factor, $\gamma^2 = 1 + p^2/(m_{\rm e}c^2)^2$, electron energy $E = (\gamma-1)\,m_{\rm e}c^2$).

2.3. Primary runaway seeds

The primary runaway seeds include Dreicer generation, hot-tail runaway generation mechanism, tritium decay and Compton scattering sources, and must take into account the impurity effects discussed in the section above.

2.3.1. Dreicer mechanism. The Dreicer mechanism produces runaways by velocity space diffusion into the runaway region. Assuming quasi-steady state for the electron distribution function, the generation rate is [25, 26]:

$$\left(\frac{{\rm d}n_{\rm r}}{{\rm d}t}\right)_{\rm Dreicer} = n_{\rm e}\nu_{\rm coll}\left(\frac{m_{\rm e}c^2}{2T_{\rm e}}\right)^{3/2}\varepsilon^{-3\,(1+Z_{\rm eff})/16} \times \exp\left(-\frac{1}{4\varepsilon} - \sqrt{\frac{(1+Z_{\rm eff})}{\varepsilon}}\right), \quad (14)$$

with $\varepsilon \equiv E_{\rm D}/E_\parallel$, $\nu_{\rm coll} \equiv n_{\rm e}e^4\ln\Lambda/4\pi\varepsilon_0^2 m_{\rm e}^2c^3$ is the collision frequency for relativistic electrons and $E_{\rm D} \equiv E_{\rm R}\cdot(m_{\rm e}c^2/kT_{\rm e})$ is the Dreicer field.

Considering the discussion on the effect of the impurities on the runaway electrons, a similar expression to equation (14) but with appropiate collisional parameters evaluated at the critical energy for runaway generation, $\gamma_{\rm c}$, is expected for the Dreicer generation of runaway electrons in plasmas with high impurity content [27]:

$$\left(\frac{{\rm d}n_{\rm r}}{{\rm d}t}\right)_{\rm Dreicer} \approx n_{\rm ef}\,\nu_{\rm coll}(\gamma_{\rm c})\left(\frac{m_{\rm e}c^2}{2T_{\rm e}}\right)^{3/2}\varepsilon(\gamma_{\rm c})^{-3\,(1+Z_{\rm coll}(\gamma_{\rm c}))/16} \times \exp\left(-\frac{1}{4\varepsilon(\gamma_{\rm c})} - \sqrt{\frac{(1+Z_{\rm coll}(\gamma_{\rm c}))}{\varepsilon(\gamma_{\rm c})}}\right), \quad (15)$$

where $\varepsilon(\gamma_{\rm c}) \equiv E_\parallel/E_{\rm D}(\gamma_{\rm c})$, $\nu_{\rm coll}(\gamma_{\rm c}) \equiv e^4\alpha_{\rm e}(\gamma_{\rm c})/4\pi\varepsilon_0^2 m_{\rm e}^2c^3$ and $E_{\rm D}(\gamma_{\rm c}) \equiv E_{\rm R}(\gamma_{\rm c})\cdot(m_{\rm e}c^2/k\,T_{\rm e})$ with $E_{\rm R}(\gamma_{\rm c}) \equiv e^3\alpha_{\rm e}(\gamma_{\rm c})/4\pi\varepsilon_0^2 m_{\rm e}c^2$ (note that, in this expression, it is taken into account than only free electrons can diffuse through the critical velocity in velocity space).

2.3.2. Hot-tail runaway generation. Hot-tail runaway electron generation in tokamak disruptions is caused by incomplete thermalization of the electron distribution function during the rapid plasma cooling in the thermal quench. Electrons at high velocities in the initial Maxwellian, for which the collision frequency is lower than the plasma cooling rate, are in a transient phase left as a hot tail of the electron distribution. The part of this tail above the runaway critical energy can easily become runaways due to the rising electric field. In contrast to other primary generation mechanisms, hot tail runaway generation is limited in time to the cooling phase, i.e. to the disruption thermal quench.

The number of runaway electrons generated by this mechanism can be obtained by solving the Fokker-planck equation for energetic electrons colliding with a Maxwellian bulk distribution with temperature T (without taking the electric field into account) and integrating the resulting distribution function over the runaway region [18, 28, 29],

$$\left(\frac{{\rm d}n_{\rm r}}{{\rm d}t}\right)_{\rm hot-tail} = 4\pi\,\frac{\rm d}{{\rm d}t}\int_{v_{\rm c}}^{\infty}(v^2 - v_{\rm c}^2) f\,{\rm d}v \quad (16)$$

where $v_{\rm c}$ is the critical velocity for runaway generation.

Here, instead, a simplified approximation will be used based on analytical estimates obtained under the assumption of an exponential decrease of the temperature [18], $T = T_0\,{\rm e}^{-t/t_0}$ (t_0 is the characteristic thermal quench duration):

$$n_{\rm r}^{\rm hot-tail} \approx n_{\rm e0}\,\frac{2}{\sqrt{\pi}}\,u_{\rm c,min}\,{\rm e}^{-u_{\rm c,min}^2} \quad (17)$$

with

$$u_{\rm c,min}^3 = t_0\nu_0\left[2\ln\frac{E_{D0}}{E_{\parallel 0}} - \frac{4}{3}\,\ln\left(\frac{4}{3}t_0\nu_0\right) - \frac{5}{3}\right] \quad (18)$$

(in these expressions, $\nu_0 = n_{\rm e0}e^4\ln\Lambda/(4\pi\varepsilon_0^2 m_{\rm e}^2 v_{T0}^3)$ is the initial (pre-disruption) collision frequency of the thermal electrons, $n_{\rm e0}$ and v_{T0} the initial background electron density and thermal speed, and $E_{D0}/E_{\parallel 0}$ is the initial ratio of the Dreicer field and parallel electric field).

Expression (17) has the advantage of being a simple analytical form, and can therefore be used to gain qualitative understanding of the hot tail generation. This expression is known to overestimate the number of high energy electrons compared with kinetic calculations, but allows to identify by its simple functional form how the hot tail runaway generation depends on the disruption parameters [18].

In the case of high impurity content, the free electron density before the rapid thermal quench, n_{e0}, will be determined by the amount of impurities injected and their state of ionization,

$$n_{e0} \approx n_H + < Z >_0 \; n_{z0} \tag{19}$$

(n_H is the hydrogen density and n_{z0}, $<Z>_0$, the density of impurities and their state of ionization before the thermal quench). On the other hand, the analytical approximation provided by equation (17) for the case of an exponential drop of the temperature, $T \approx T_0 \exp(-t/t_0)$, assumes a constant electron density and Z_{eff} during the rapid temperature fall [18]. However, during the thermal quench, at the same time that the temperature drops, the amount of impurities as well as their ionization state may also change. Based on the evaluation carried out in [18] and taking into account the effect of the impurities on the runaway electron dynamics, a better approximation to the hot-tail runaway seed is obtained replacing, in the estimate of $u_{c,min}$ (equation (18)), $(n_{e0} \ln\Lambda_0)$ by $\alpha_{e,f}$, and Z_{eff} by $Z_{coll,f}$, where $\alpha_{e,f}$ and $Z_{coll,f}$ would be the values of α_e and Z_{coll} at the critical energy at the end of the thermal quench.

2.3.3. Tritium decay. Tritium decays into helium-3 by a beta decay process:

$$T \rightarrow \; {}^3_2\mathrm{He} + e^- + \overline{\nu}_e,$$

($\overline{\nu}_e$ is the electron antineutrino) with a half-life $\tau_T = 4500 \pm 8$ d. Therefore, the production rate of beta-electrons can be written

$$\left(\frac{dn_\beta}{dt}\right)_T = \lambda_T \, n_T = \ln 2 \, \frac{n_T}{\tau_T} \tag{20}$$

(n_T is the tritium density and $\lambda_T = \ln 2/\tau_T$ is the tritium disintegration rate constant). Only the beta-electrons in the tritium beta-decay energy spectrum with an energy larger than the runaway critical energy will contribute to the primary runaway seed. Thus, the runaway generation rate due to the tritium decay might be estimated

$$\left(\frac{dn_r}{dt}\right)_T \approx n_T \, \nu_T(E_c) = \ln 2 \, \frac{n_T}{\tau_T} \, F_\beta(E_c), \tag{21}$$

where $\nu_T(E_c) = \ln 2 \cdot F_\beta(E_c)/\tau_T$ and

$$F_\beta(E_c) = \int_{E_c}^{E_{max}} f_\beta(E) \, dE, \tag{22}$$

is the fraction of the beta-spectrum that would become runaway ($f_\beta(E)$ is the beta-energy spectrum normalized to one, E_c the critical runaway energy, determined including the effect of the collisions with the background plasma and the impurity ions [23], and E_{max} the maximum energy of the beta-electrons, $E_{max} = 18.6$ keV).

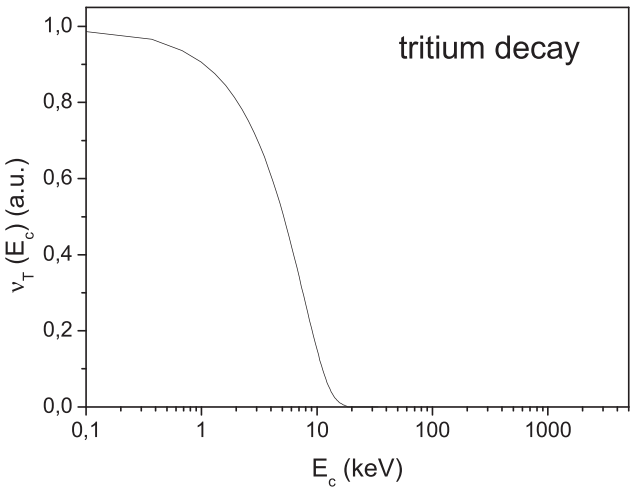

Figure 1. $\nu_T \equiv (1/n_T) \cdot (dn_r/dt)_T$ versus the critical energy for runaway generation, E_c (normalized to one at $E_c = 0$).

The dependence of the runaway growth rate due to tritium decay on the critical energy for runaway generation, E_c, is illustrated in figure 1 which shows ν_T as a function of E_c (normalized to one at $E_c = 0$). The shape of $\nu_T(E_c)$ is determined by the beta-energy spectrum, dropping sharply after only a few keV's and becoming zero for $E_c > 18.6$ keV (maximum energy of the beta-electrons).

2.3.4. Compton scattering. The runaway production rate associated with the Compton scattered electrons by the γ rays emitted by the activated walls by DT produced neutrons in ITER can be approximated:

$$\left(\frac{dn_r}{dt}\right)_{compton} \approx n_e \int \Gamma_\gamma(E_\gamma) \, \sigma(E_\gamma) \, dE_\gamma. \tag{23}$$

Here E_γ is the photon energy, $\Gamma_\gamma(E_\gamma)$ the gamma energy flux spectrum and $\sigma(E_\gamma)$ the Compton cross-section for photons of energy E_γ.

As an estimate for the gamma flux energy spectrum, an average of the calculations performed at four different poloidal locations in ITER using radiation transport calculations [30] will be used, which can be fitted to (see figure 2):

$$\Gamma_\gamma(E_\gamma) \propto \exp\left(-\exp(-z) - z + 1\right) \text{ with } z \equiv \frac{\ln(E_\gamma(\mathrm{MeV})) + 1.2}{0.8}. \tag{24}$$

This estimate may be considered adequate for the intended purpose of this paper although the details of the spectra will depend on the final configuration of the first wall and blanket.

There is a contribution to the gamma flux which does not depend on the fusion power as it corresponds to a time integrated activation of the walls, and the typical ratio between prompt during plasma burn and larger timescale decay (between pulses) gamma fluxes is of the order of 1000 [30]. Thus, we assume a worst case scenario in which the gamma flux during the disruption is at a similar level to that during burning plasma conditions, which scales with fusion power. This is a reasonable assumption even taking into account that the prompt gamma fluxes can decay or change their spectrum during the

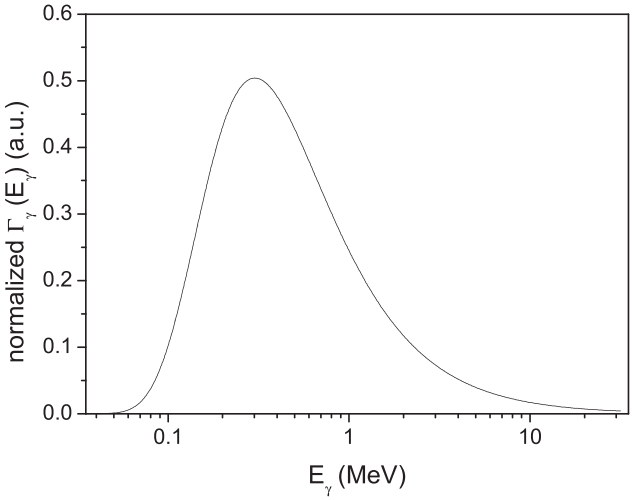

Figure 2. Normalized gamma flux energy spectrum in ITER [30].

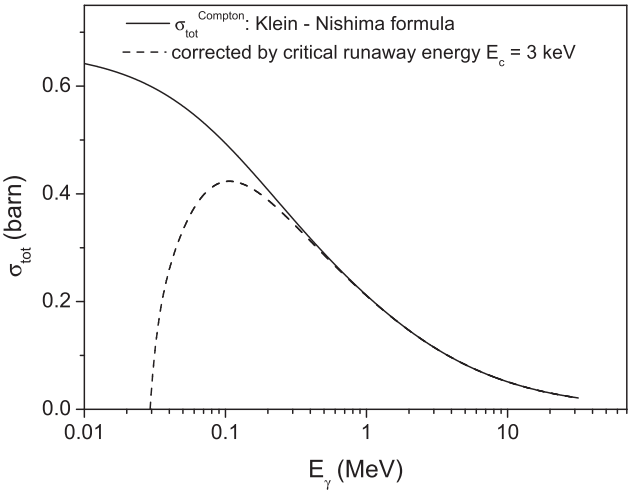

Figure 3. Compton cross section as a function of the photon energy. Full line: integrated over all the deflection angles; dashed line: integrated only over scattered electrons with an energy larger than $E_c = 3$ keV.

disruption current quench. Compton scattered electrons can have energies up to a few MeVs and collisional relaxation times to a few tens of milliseconds. Therefore, a substantial fraction of the electrons due to the prompt gamma fluxes just before the thermal quench can survive and dominate the initial seed after the thermal quench and, hence, the runaway avalanche growth during the current quench. The total gamma flux is evaluated to be $\approx 10^{18}$ m^{-2} s^{-1} for an H-mode discharge at 15 MA and 500 MW fusion power [30, 31]. At lower currents, the gamma flux is scaled with the fusion power. Taking into account that, for ITER plasmas which have a high temperature, the fusion power scales with the square of the plasma energy and this with $\sim I_p^{3/2}$ from the ITERH98 scaling law [32], the total gamma flux would scale like $\sim I_p^3$. For L-mode cases, as the plasma energy is about half that of the H-mode at the same current, the total gamma flux would be $\sim 1/4$ the corresponding H-mode plasma at the same current.

The total Compton cross-section, $\sigma(E_\gamma)$, for a given photon energy, E_γ, can be obtained integrating the Klein–Nishina differential cross-section [33]:

$$\frac{\mathrm{d}\sigma}{\mathrm{d}\,\Omega} = \frac{r_e^2}{2}\frac{E_\gamma'^2}{E_\gamma^2}\left(\frac{E_\gamma}{E_\gamma'} + \frac{E_\gamma'}{E_\gamma} - \sin^2\theta\right), \tag{25}$$

where $r_e = e^2/4\pi\varepsilon_0 m_e c^2$ is the classical electron radius and θ, E_γ', are the deflection angle and the energy of the scattered photon, respectively:

$$E_\gamma' = \frac{E_\gamma}{1 + \frac{E_\gamma}{m_e c^2}(1 - \cos\theta)}. \tag{26}$$

The integration should be performed over deflection angles larger than the critical angle, θ_c, corresponding to an energy of the scattered electrons $E_e = E_\gamma - E_\gamma' = E_c$, as only scattered electrons with an energy larger than the critical energy, E_c, will become runaways,

$$\cos\theta_c = 1 - \frac{m_e c^2}{E_\gamma}\frac{E_c/E_\gamma}{1 - (E_c/E_\gamma)}, \tag{27}$$

so that,

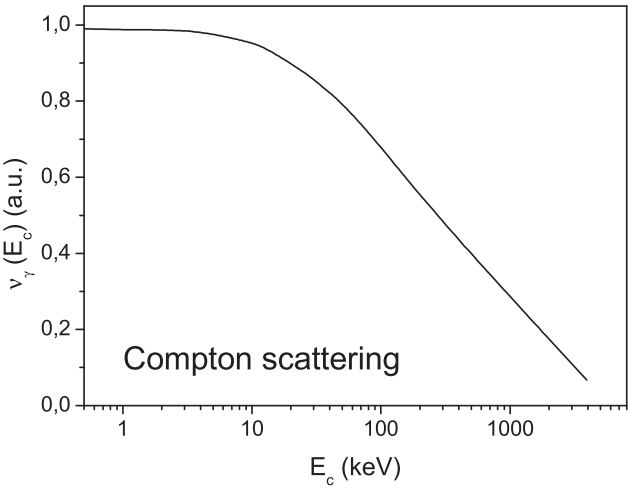

Figure 4. $\nu_\gamma \equiv (1/n_e)\cdot(\mathrm{d}n_r/\mathrm{d}t)_{\mathrm{compton}}$ versus the critical energy for runaway generation, E_c (normalized to one at $E_c = 0$).

$$\sigma(E_\gamma) = \int_{\theta_c}^{\pi} \frac{\mathrm{d}\sigma}{\mathrm{d}\,\Omega}\,\mathrm{d}\,\Omega\,, \tag{28}$$

which, using $\mathrm{d}\,\Omega = 2\pi\,\sin\theta\,\mathrm{d}\theta$ together with equations (25) and (26), yields

$$\sigma(E_\gamma) = \frac{3\,\sigma_T}{8}\left\{\frac{x^2 - 2x - 2}{x^3}\,\ln\frac{1 + 2x}{1 + x\,(1 - \cos\theta_c)} + \frac{1}{2x}\left[\frac{1}{[1 + x\,(1 - \cos\theta_c)]^2} - \frac{1}{(1 + 2x)^2}\right] - \frac{1}{x^3}\left[1 - x - \frac{1 + 2x}{1 + x\,(1 - \cos\theta_c)} - x\,\cos\theta_c\right]\right\}, \tag{29}$$

with $x \equiv E_\gamma/m_e c^2$ and $\cos\theta_c$ given by equation (27). An example is shown in figure 3 which compares the total cross section integrated over all the deflection angles with that obtained integrating only over scattered electrons with an energy larger than the critical energy and assuming $E_c = 3$ keV.

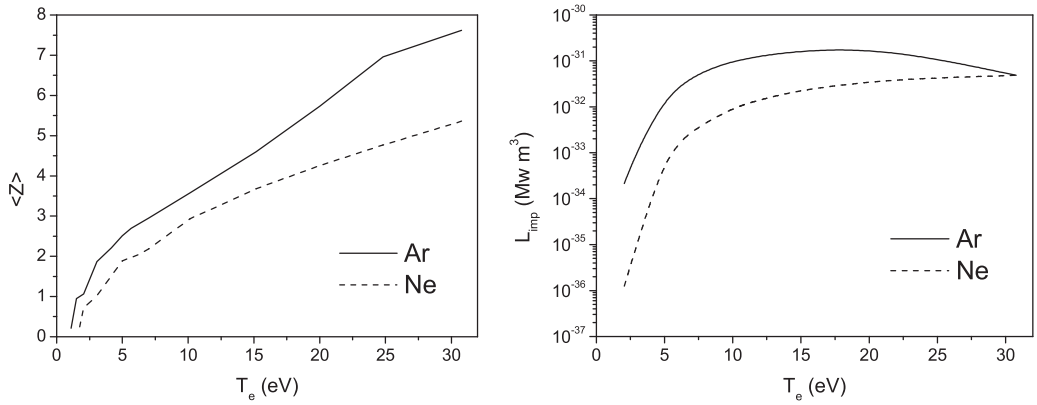

Figure 5. $L_{\rm imp}(T_{\rm e})$ and $\langle Z\rangle(T_{\rm e})$ for Ar and Ne used in this work (ADAS atomic data base).

The dependence of the runaway production due to Compton scattering on $E_{\rm c}$ is illustrated in figure 4 which shows $\nu_\gamma(E_{\rm c}) \equiv \int \Gamma_\gamma(E_\gamma)\,\sigma(E_\gamma)\,{\rm d}E_\gamma\ [({\rm d}n_{\rm r}/{\rm d}t)_{\rm compton} \approx n_{\rm e}\,\nu_\gamma(E_{\rm c})]$ (normalized to one at $E_{\rm c}=0$) as a function of $E_{\rm c}$. The function $\nu_\gamma(E_{\rm c})$ shows a far more gradual drop with $E_{\rm c}$ than $\nu_{\rm T}(E_{\rm c})$ for the tritium decay so that, in contrast to the tritium seed, it might give a noticeable contribution for substantially large $E_{\rm c}$ values.

Due to the large energy of the gamma-ray photons ($\sim$0.1–10 MeV) emitted by the activated ITER wall compared with the electron binding energies for Ar and Ne, both free and bound electrons can be Compton scattered and, therefore, the total electron density, $n_{\rm e,tot} = n_{\rm ef} + n_{\rm eb}$, is used in the evaluation of the runaway seed due to Compton scattering, i.e. $n_{\rm e,tot}$ is used in equation (23). In addition, the effect of the collisions with the impurities on the critical energy and, thus, on $\sigma(E_\gamma)$ (equation (29)), is included to evaluate the Compton seed in our studies.

3. Analysis of iter scenarios

3.1. Formation of the runaway beam

We have carried out the analysis of runaway beam formation and termination in ITER disruptions by applying the 1D model described above for selected plasma conditions ranging from 5 MA to 15 MA DT pre-disruption H-mode and L-mode plasmas. In this paper, we will focus on the results for H-mode plasmas as they have the largest seeds due to their higher temperatures and fusion production. Mitigated disruptions by Ar and Ne injection are considered. The amount of injected impurities has been varied while ensuring that the exponential decay time for the current quench is kept within the range for acceptable mechanical loads on the ITER vessel and in-vessel components [34].

For each plasma condition studied, the methodology used for our analysis can be summarized as follows:

1. Initial plasma current and profile shape:
   This is the plasma current just after the thermal quench. An increase $\leqslant$10–15% over the nominal pre-disruption plasma current is assumed to account for the flattening of the current profile at the start of the disruption which leads to the usual positive current spike by magnetic flux conservation in ITER disruptions [35]. For the initial current density profile, the parametrization $j(r) = j_0\,[1-(r^2/a^2)]^\nu$ is applied. A flattish current profile, $l_{\rm int}\sim 0.7$ ($l_{\rm int}$ is the internal plasma inductance), is considered, corresponding to an internal flux inductance $L_{\rm int}\sim 5\ \mu$H. The initial runaway current is assumed to be zero: $j_{\rm r}(0,r)=0$.
2. Thermal plasma and impurities properties:
   For simplicity, the temperature and density profiles are assumed to be flat and constant in time during the disruption current quench. The density of hydrogenic species (deuterium plus tritium) is given by the pre-disruption plasma conditions studied. For a given impurity (Ar or Ne) density, n_z, $T_{\rm e}$ is obtained using the power balance equation

$$\eta\, j_{\rm OH}^2 = n_{\rm ef}\, n_z\, L_{\rm imp}, \tag{30}$$

   where $n_{\rm ef} = n_{\rm H} + <Z>\cdot n_z$ is the free electron density, $n_{\rm H}$ is the pre-disruption deuterium + tritium density, $<Z>(T_{\rm e})$ the averaged impurity charge, $j_{\rm OH}$ is the ohmic current density and $L_{\rm imp}(T_{\rm e})$ the radiative cooling rate. The typical times for Ne and Ar to reach coronal equilibrium for the conditions expected after the thermal quench in ITER are in the range of 5–10 ms, which are shorter than the current quench times considered. Therefore, for the modelling presented in this paper, we assume that the impurities are in coronal equilibrium during the current quench and the atomic data are taken from the ADAS database [36]. The corresponding radiative cooling rates, $L_{\rm imp}(T_{\rm e})$, and averaged impurity charges, $<Z>(T_{\rm e})$, for Ar and Ne used in this work are shown in figure 5. Opacity effects have not been considered. Nevertheless, the calculations performed in [37] show that opacity effects are significant for Be- and C-seeded plasmas in ITER but the influence of opacity on current decay times is not so significant for Ar and Ne-seeded plasmas.
   The resulting current decay rate must be consistent with acceptable forces on the ITER vessel and in-vessel components (exponential current quench time, $\tau_{\rm res}\sim$ 22–66 ms for 15 MA disruptions [34]) which determines

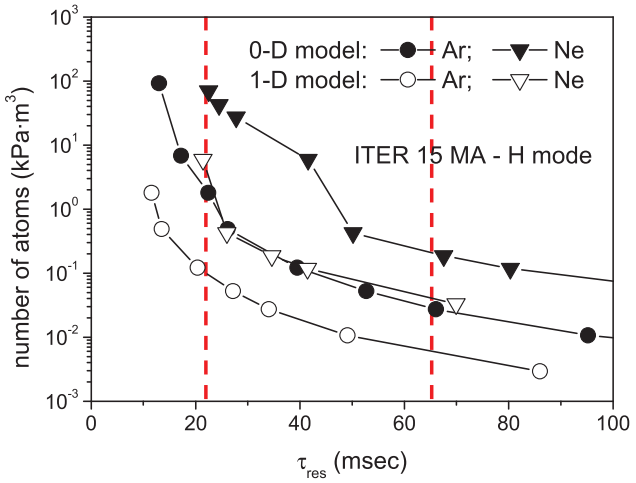

Figure 6. Comparison between the 0D (black symbols) and 1D (open symbols) evaluations of the number of injected atoms (in kPa · m^3) assuming 100% assimilation efficiency versus τ_{res} for Ar (circles) and Ne (triangles) (15 MA current and $n_H = 10^{20}$ m^{-3}). The vertical red dashed lines indicate the range of τ_{res} values leading to acceptable forces onto the vessel and in-vessel components in ITER.

the impurity density for a given n_H. In this respect, it is important to note that evaluating τ_{res} by applying a 0D modeling of the current decay [34, 38] according to

$$\tau_{res} \approx \frac{La^2}{2R_0\,\eta}, \tag{31}$$

which assumes fixed L during current decay, results in a substantial overestimate of the amount of the impurities required to obtain a given τ_{res} in comparison with 1D simulations of the current quench which allow for the evolution of the current profile and changes in the plasma inductance, L, during the current decay. This is illustrated in figure 6 which compares, for a 15 MA disruption and $n_H = 10^{20}$ m^{-3}, Ar (circles) and Ne (triangles), the 0D (black symbols) and 1D (open symbols) estimates of the number of injected atoms (in kPa · m^3) assuming 100% assimilation efficiency versus τ_{res}. The estimates obtained with the 1D model applied in this paper are consistent with recent results of free boundary equilibrium calculations of disruption current quenches accounting for the development of VDEs [39]. The main deviations are found for the lowest T_e (shortest τ_{res}) and are due to the differences between the ADAS atomic data here used and those from the ZIMPUR code used in [39] for the impurity dynamics. The largest amount of impurities is found for the shortest τ_{res} (∼22 ms) which for the case of Ar requires ∼0.1 kPa · m^3 (plasma temperature $T_e \sim 4$ eV) while, in the case of Ne, with a much lower radiation rate at low T_e, it requires ∼6 kPa · m^3 (plasma temperature $T_e \sim 3$ eV).

3. Primary and secondary runaway sources:
   The formation of the runaway population takes place place by the generation of a runaway seed (including the Dreicer, hot-tail, tritium and Compton scattering sources) at the start of the current quench (during the thermal quench in the case of the hot-tail seed) followed by the avalanche amplification of the runaway seed along the current quench. To evaluate these processes we use the thermal plasma and impurity parameters discussed above.
4. Radial runaway losses:
   During the current quench phase, no runaway losses are considered ($\tau_L \to \infty$), which corresponds to the most pessimistic case regarding the formation of the runaway electrons in ITER.
5. Modelling:
   The modelling of the current quench phase of the disruption is carried out solving the system of equations (2)–(3) which takes into account the evolution of the plasma and runaway current density profiles.
6. Output:
   The model evaluates in a fully self-consistent way the runaway current, the kinetic energy of the runaway beam, the runaway current and energy density profiles, and the runaway energy spectrum versus time after the thermal quench. We typically show the results in this paper at the expected time in ITER for the vertical instability growth. This instability leads to the termination of the runaway formation phase following the vertical displacement event (VDE), which typically occurs at ∼100 ms [40].

3.1.1. Primary runaway sources. The runaway primary sources are evaluated locally using the approaches described in section 2.3, including the effect of the collisions with the impurity ions (section 2.2). Figure 7 shows typical Compton and tritium seed profiles, corresponding to an ITER disruption at 15 MA with Ar injection and $\tau_{res} = 34$ ms. The Compton and tritium seed profiles are typically quite flat, particularly for the case of the Compton seed.

The case of the hot-tail runaway generation mechanism is remarkably different. The hot-tail source is very sensitive to the relation between the pre-disruption collision frequency of the thermal electrons ($\nu_0 \propto T^{-3/2}$) and the characteristic plasma cooling time during the thermal quench, t_0 (plasma cooling which in our estimates is assumed to be exponential in time, $T = T_0\,e^{-t/t_0}$), which for ITER is expected to be in the range 1–5 ms [41]. Therefore, local variations in the pre-disruption temperature profile can lead to strong radial variations in the resulting runaway seed, the largest seed values being found for the highest pre-disruption temperatures. This is illustrated in figure 8, which shows the estimated hot-tail runaway seeds for a 15 MA H-mode disruption (average pre-disruption temperature $\langle T \rangle = 10$ keV, and temperature profile $T(r) = 20 \times [1 - (r^2/a^2)]$ keV), and $\tau_{res} = 34$ ms, for two different cooling times, $t_0 = 1$ ms (left picture) and $t_0 = 3$ ms (right picture). The resulting seed profiles from hot-tail generation are quite peaked in the center and their magnitude depends strongly on t_0.

The dependence of the calculated runaway seed currents, I_{seed}, on the critical energy, E_c, for the analyzed scenarios (τ_{res} ∼22–66 ms) for 15 MA H-mode disruptions with Ar (black symbols) and Ne (green symbols) injection is shown in figure 9 (right). The figure to the left shows the calculated

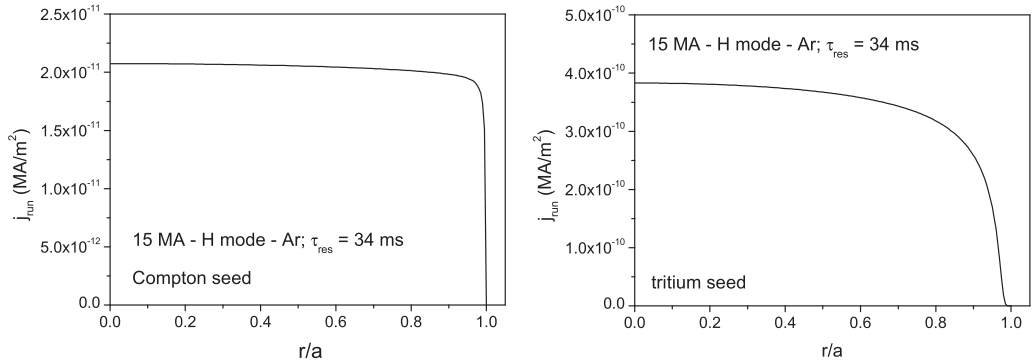

Figure 7. Compton (left) and tritium (right) runaway seed current density profiles for a 15 MA ITER disruption with Ar injection and $\tau_{res} = 34$ ms.

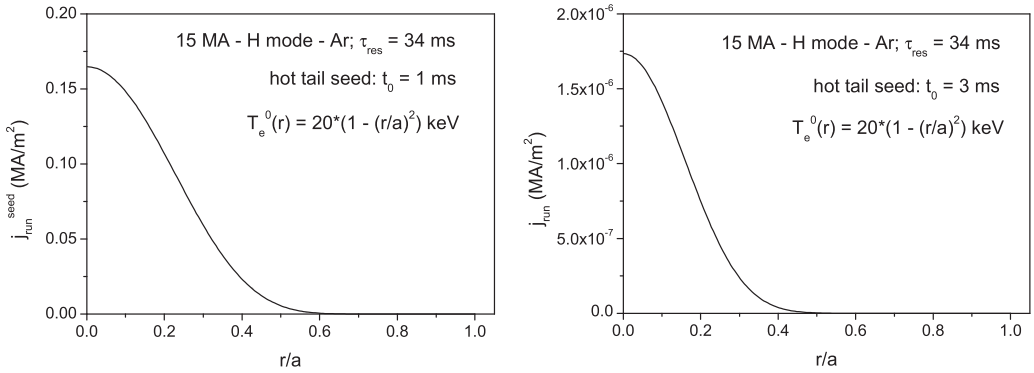

Figure 8. Hot-tail runaway seed profiles for $t_0 = 1$ ms (left) and $t_0 = 3$ ms (right), for a 15 MA ITER disruption with Ar injection, $\tau_{res} = 34$ ms and a pre-disruption temperature profile $T(r) = 20 \times [1 - (r^2/a^2)]$ keV.

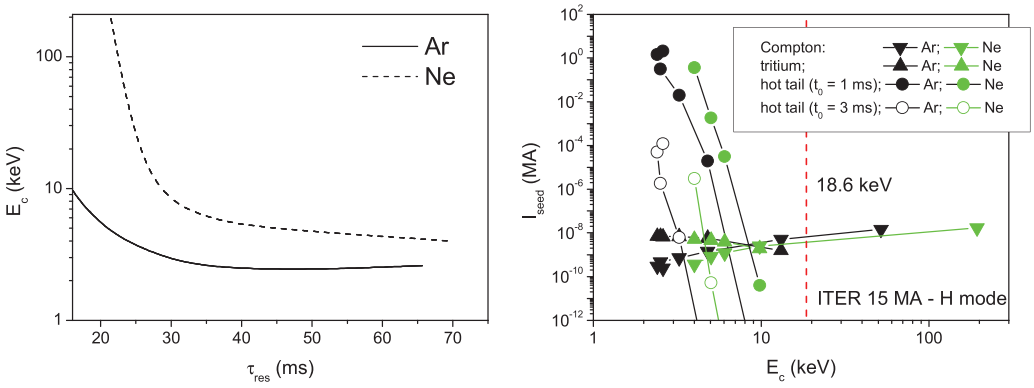

Figure 9. Left: E_c versus τ_{res} for 15 MA H-mode disruptions with Ar (full line) and Ne (dashed line) impurities; right: I_{seed} versus E_c for 15 MA H-mode disruptions, Ar and Ne impurities, for the different seed mechanisms (except the Dreicer mechanism which is negligible).

E_c as a function of τ_{res}. The critical energy decreases when τ_{res} increases and is larger for Ne than for Ar as the amount of injected impurities is larger for the lowest τ_{res} and for Ne than for Ar. The figure on the right shows that the hot-tails seeds are substantially larger than the tritium and Compton seeds, decreasing rapidly with E_c. Only when E_c has increased to large enough values (~5–10 keV for the case of the hot-tail mechanism with $t_0 = 1$ ms), the Compton and tritium seeds may become dominant. Also, the production of seed electrons through tritium decay and Compton scattering can be important if all of the magnetic surfaces are broken for a sufficient time for all high-energy electrons to be lost, but the magnetic surfaces are reestablished before the plasma current has decayed to a low value. The figure also indicates that, for the lowest E_c, the tritium process is more important than the Compton mechanism. Nevertheless, while the tritium seed decreases when E_c increases and is zero for $E_c > 18.6$ keV (see figure 1), the generation of seed runaways due to Compton scattering continuously increases with E_c. This is due to the slow drop of $\nu_\gamma(E_c)$ with E_c (figure 4) whereas the number of electrons that can be Compton scattered ($n_{e,tot} \approx n_{ef} + n_{eb}$) increases with E_c (when the number of impurity atoms is larger): $(dn_r/dt)_{compton} \approx n_{e,tot}\, \nu_{gamma}(E_c)$.

The calculated Dreicer contribution (equation (15)) appears to be negligible in comparison with all the other primary

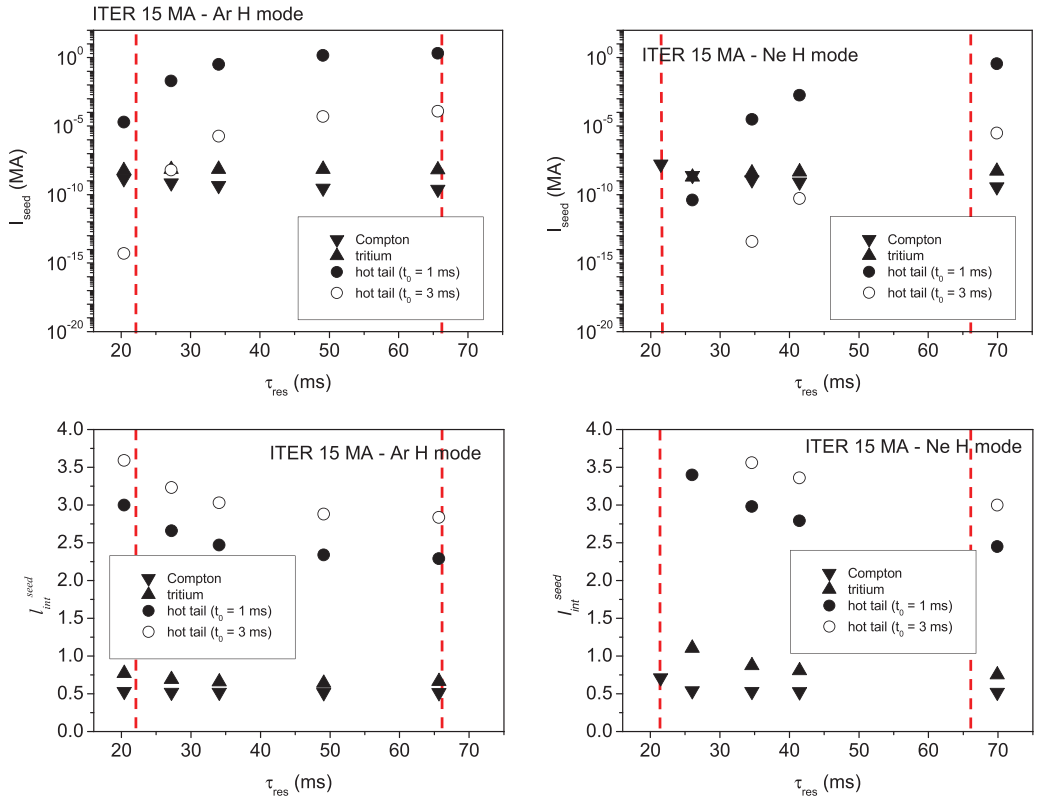

Figure 10. For 15 MA ITER disruptions with Ar and Ne injection: predicted runaway seed current (top) and internal inductance (bottom) versus current quench time (τ_{res}) for all seed mechanisms considered. The vertical red dashed lines indicate the range of τ_{res} values leading to acceptable forces onto the vessel and in-vessel components in ITER.

sources under typical ITER plasma conditions. The Dreicer generation rate depends exponentially on $\varepsilon(\gamma_c) \equiv E_D(\gamma_c)/E_\parallel$ (section 2.3.1) which is found to be in the range of a few 10^{-3} and below, too low to yield substantial runaway production in ITER disruptions.

The resulting variation of the magnitude of the runaway seeds with the current quench time is shown in figure 10 (top). For Ar, for which the impurity content (E_c) is relatively low, the Compton and tritium seeds do not change noticeably with τ_{res}, while the hot-tail seed, more sensitive to the plasma collisionality, increases with τ_{res} (lower E_c) saturating for $\tau_{res} > 40$ ms. For Ne, with a much lower radiation rate, the impurity content (and E_c) is substantially larger and for the shortest τ_{res} (largest E_c) only the Compton scattering produces a non-negligible seed. For $\tau_{res} \sim 22$ ms, the critical energy for runaway generation, E_c, is larger than the maximum energy of the emitted beta electrons during tritium decay ($E_{max} = 18.6$ keV) and the plasma is so collisional that the hot-tail contribution is negligible. When τ_{res} increases (larger temperature, lower Ne impurity density and lower E_c), the collisionality decreases and the tritium and, particularly, the hot-tail seeds increase. Figure 10 bottom shows the internal inductance of the runaway seeds as a function of τ_{res}, which provides information on the shape of the seed runaway current density profile. As it was shown in [9] (and it will be also discussed below), the shape of the runaway seed profile has an influence on the runaway current density profile generated during the disruption current quench. Tritium and, especially, Compton seeds are generally quite flat (small l_{int}), while the hot-tail seeds are strongly peaked (large l_{int}), the peaking decreasing when τ_{res} increases (i.e. for the larger seed currents).

3.1.2. Runaway current and energy. The predicted runaway current, I_r, due to the avalanche multiplication of the runaway seeds and the corresponding runaway beam energy,

$$W_{run} = \int dt' \int j_r \, (E_\parallel - E_R) \, dv, \qquad (32)$$

at the expected time for the vertical instability growth in ITER (~100 ms) are shown as a function of τ_{res} in figure 11 for 15 MA H-mode disruptions with Ar impurity. The predictions for the different runaway generation primary mechanisms are compared (except for the Dreicer mechanism which always gives a negligible contribution). When few (or all) of these mechanisms are acting together, the final result is dominated by the largest one. The Compton and tritium seeds yield typically final runaway currents ~4 MA with energies ~10 MJ. The largest runaway formation is caused by the hot-tail mechanism for the shortest cooling time ($t_0 = 1$ ms) which, increasing with τ_{res} when the impurity content decreases, can lead to substantial runaway generation ~10 MA with $W_{run} \sim 20$ MJ for the largest τ_{res}. For Ne injection (figure 12), the predicted runaway formation is negligible for the shortest τ_{res} due to the large impurity content, increasing with τ_{res} to ~4 MA and ~10 MJ for the Compton and tritium seeds, and to ~10 MA with $W_{run} \sim 20$ MJ for the hot-tail mechanism with $t_0 = 1$ ms.

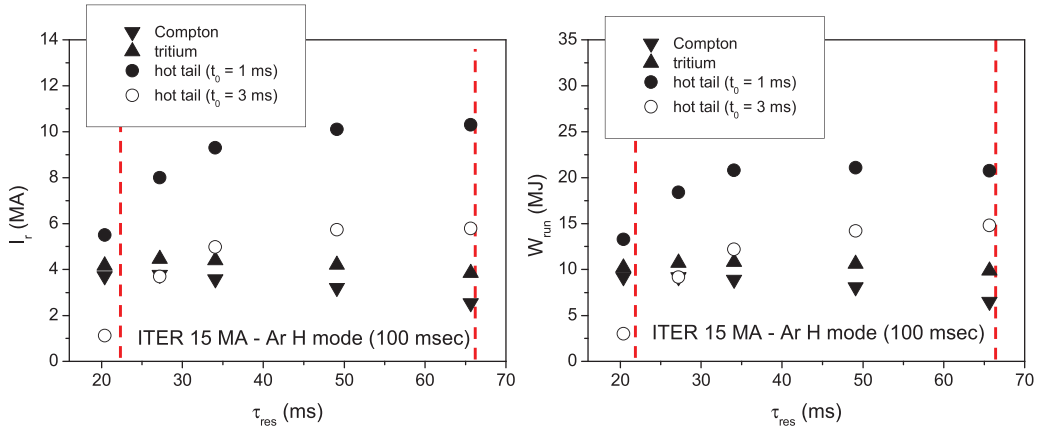

Figure 11. Predicted runaway current and runaway beam energy at 100 ms versus τ_{res} for 15 MA H-mode disruptions and Ar impurity for all seed mechanisms (except the Dreicer mechanism which is negligible).

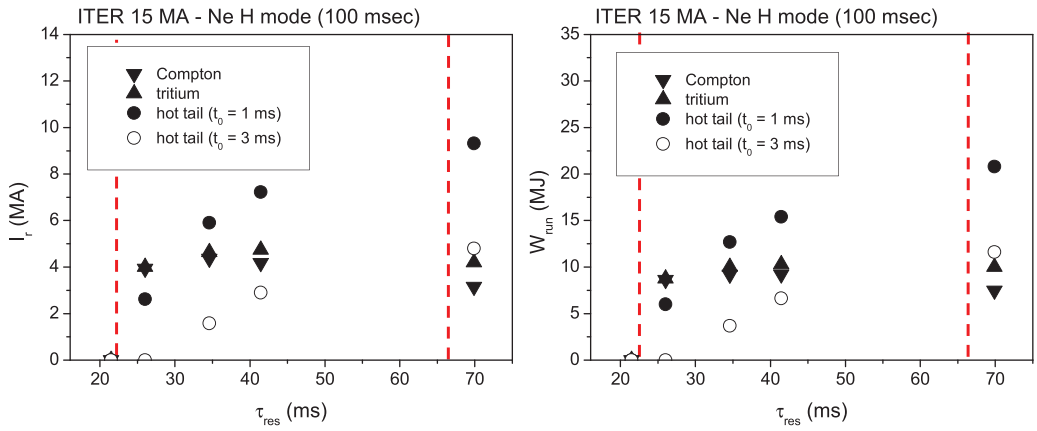

Figure 12. Predicted runaway current and runaway beam energy at 100 ms versus τ_{res} for 15 MA H-mode disruptions and Ne impurity for all seed mechanisms (except the Dreicer mechanism which is negligible).

Figure 13 shows the results for the predicted runaway current at 100 ms as a function of the runaway seed current (black symbols: Ar injection; green symbols: Ne injection). The figure indicates that, while the range of variation of I_{seed} for the Compton and tritium seeds is relatively small leading to typical runaway currents ~4 MA, the hot-tail mechanism is strongly sensitive to the rate of the temperature drop (quantified by means of t_0) and to the amount of impurities delivered into the plasma, determined by the rate of impurity mixing into the ITER plasma which is not modeled here, leading to a much broader range of variation for the runaway seed and the generated runaway current. The figure also suggests that I_r scales with $\sim \ln I_{seed}$ in agreement with analytical predictions for the avalanche multiplication of a runaway seed [23].

The number of e-folds required in the avalanche process to transfer the plasma current to the runaway electrons (avalanche gain G_{av}, $I_r = I_{seed}\, e^{G_{av}}$) is plotted in figure 14 (left) as a function of the critical energy, E_c, for the analyzed scenarios and the different runaway seeds. The more e-folds that are required (larger G_{av}), the less current in the runaway electrons (right figure). Only those scenarios which do not lead to the formation of a runaway plateau, typically because of a large enough collisionality (and, hence, E_c), can depart from this general trend (this is the case, for example, of the hot-tail

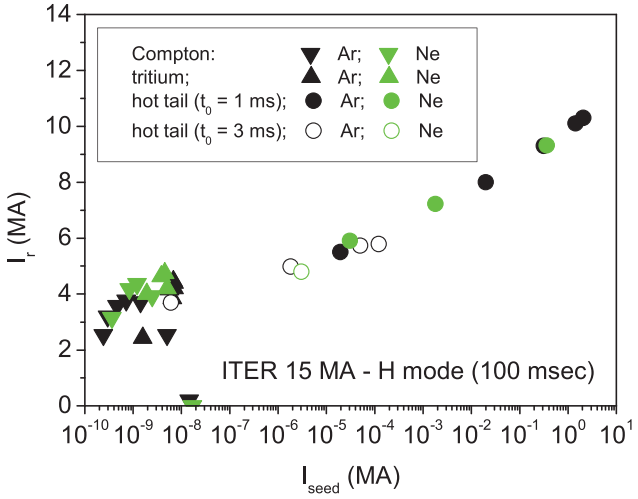

Figure 13. Predicted runaway current at 100 ms versus I_{seed} for 15 MA H-mode disruptions, Ar and Ne impurities, for all seed mechanisms (except the Dreicer mechanism which is negligible).

scenarios in the figure with negligible runaway formation, for which $E_c > 50$ keV).

The main dependence of I_r and W_{run} is found on the pre-disruption plasma current which is illustrated in figure 15 for Ar injection for a range of currents ~5–15 MA. For the lowest

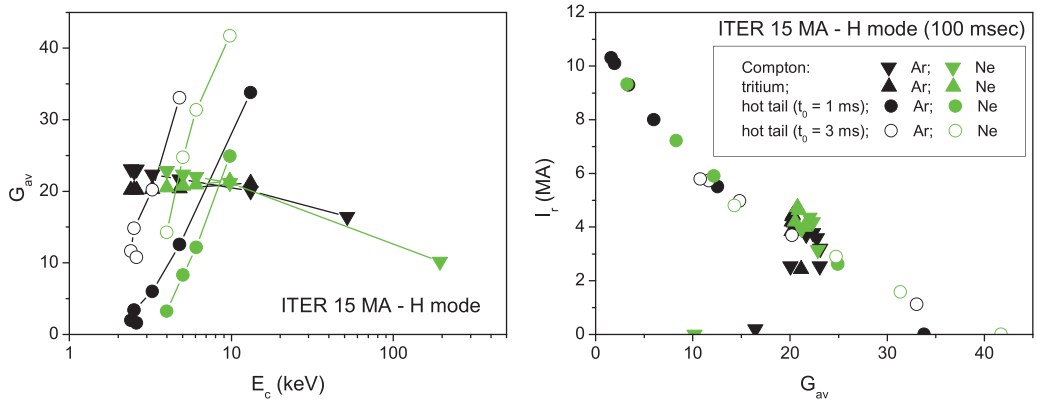

Figure 14. Left: avalanche gain, G_{av}, versus critical energy, E_c, for 15 MA H-mode disruptions with Ar (black symbols) and Ne (green symbols) impurities and for the different seed mechanisms (except Dreicer generation); right: I_r at 100 ms versus G_{av} for the same scenarios.

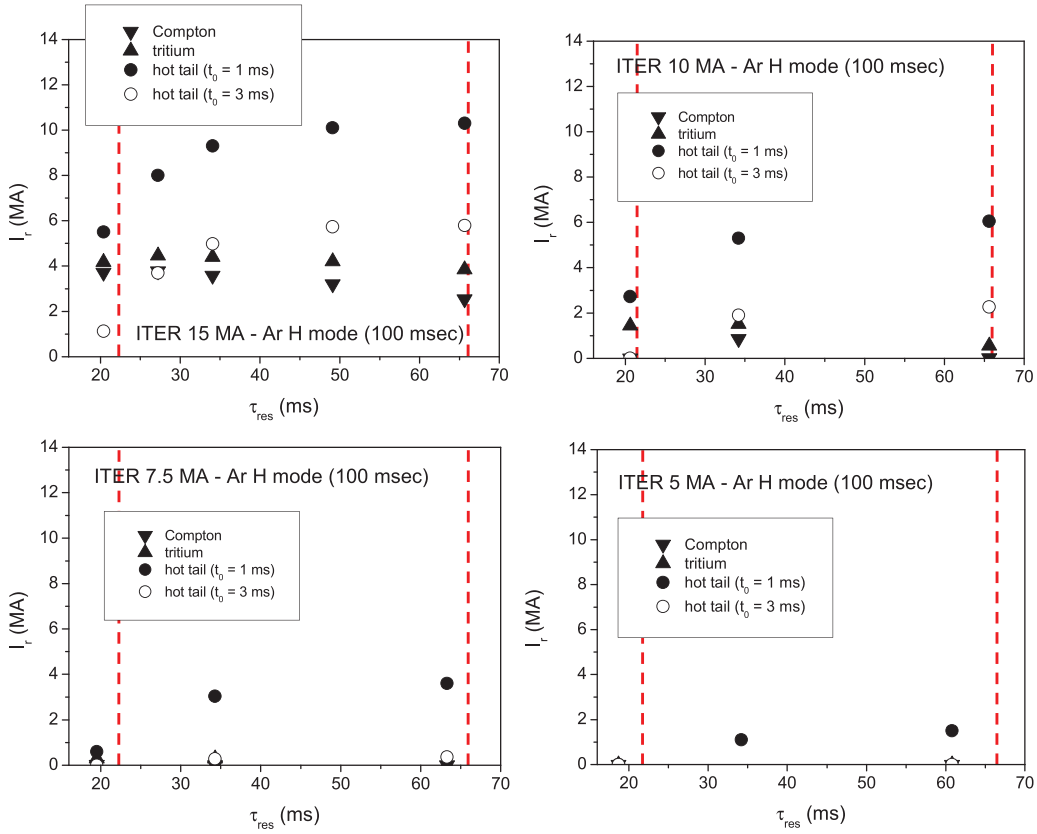

Figure 15. Predicted runaway current at 100 ms versus τ_{res} for 15 MA H-mode disruptions with Ar impurity: top: 15 MA and 10 MA H-mode cases; bottom: 7.5 MA and 5 MA H-mode cases. The vertical red dashed lines indicate the range of τ_{res} values leading to acceptable forces onto the vessel and in-vessel components in ITER.

τ_{res}, due to the large impurity content required, the runaway production is negligible for $I_p \leqslant 7.5$ MA. For the largest τ_{res}, the predicted runaway current decreases substantially with the pre-disruption plasma current and is already very small under 5 MA.

These trends in I_r and W_{run} evaluated with our 1D model are similar to those found by means of a zero-dimensional model of the disruption [38]. However, the one-dimensional predictions tend to lead to a larger runaway current than the 0D estimates for the shortest current quenches, as a result of the substantially lower impurity densities required to achieve a given τ_{res} in 1D modelling compared to 0D (as shown in the beginning of section 3.1). In contrast, for the longest current quenches, for which the amount of impurities is low both in the 1D and 0D analysis, the predicted runaway currents and energies by the one-dimensional analysis are smaller. As discussed in [9], this is mainly due to the fact that in the 1D calculations the runaway electrons are mostly generated in the central region of the plasmas where, although the electric field is larger than in the 0D model, the available volume is substantially smaller [9].

The runaway current and energy density profiles obtained in our 1D model are found to be roughly proportional and, therefore, the average runaway kinetic energy is closely constant

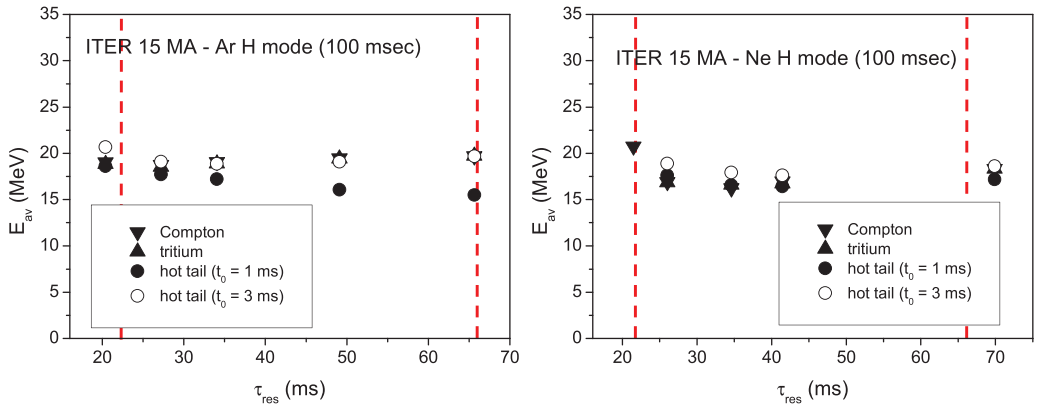

Figure 16. Average kinetic energy of the runaway electrons at 100 ms versus τ_{res} for 15 MA H-mode disruptions and Ar (left) and Ne (right) impurities. The vertical red dashed lines indicate the range of τ_{res} values leading to acceptable forces onto the vessel and in-vessel components in ITER.

across the profile. This is due to the fact that, to a great extent, the runaway energy distribution function, dominated by avalanche and having neglected the electron synchrotron radiation losses, is similar at all radii, exponentially decaying with energy, $f_{run} \sim \exp(-E/T_r)$, with an average energy [23],

$$E_{av} \sim T_r \equiv \frac{m_e c^2\, \alpha_e(\gamma_c)\, a(Z_{coll}(\gamma_c))}{n_{e,tot}}. \qquad (33)$$

Figure 16 shows, for the same cases that figures 11 and 12, the average kinetic energy, E_{av}, of the runaway electrons as a function of τ_{res} at 100 ms. The values of E_{av} typically range from 15 to 20 MeV in all the ITER cases modelled in our studies.

3.1.3. Runaway current profile shape. Beam stability Figure 17 (left) shows an example of the runaway current density profile at the plateau phase (full line) for a 15 MA H.mode disruption with Ar impurity, hot tail seed with $t_0 = 1$ ms and $\tau_{res} = 34$ ms, which leads to the generation of a substantial runaway current ~9 MA. The initial current density profile, $j_p^0(r)$, at the start of the current quench (dashed line) is also included for comparison, and the calculated safety factor profile, $q(r)$, at the plateau phase is shown in figure 17 (right). The resulting runaway current profile is flattened in the central region but overall is more peaked than the initial plasma current profile ($l_{int} \sim 1.7$ in contrast to $l_{int}^0 \sim 0.74$), while $q(0) \sim 1$. Note that the q profile shown in figure 17 (right) is the cylindrical q and that the resulting value of q at $r = a$ (~3.4) is lower than for the real plasma. With a more realistic approximation for plasma equilibrium, this value must be corrected by a geometrical factor so that $q(r = a) \sim 3$ for a 15 MA current, which, in this case, would lead to $q_a \equiv q(a) \sim 5$ for the plateau runaway beam.

The central peaking of the runaway current density profile during the disruption current quench is a well-known feature of runaway beam formation during disruptions which has been theoretically predicted in [11, 12], experimentally confirmed in [4, 10] and analyzed in detail in [9]. As it was discussed in [11], such a peaking could be understood from the interplay between runaway generation and radial diffusion of the electric field. When the runaway electrons are generated in the central region of the plasm, the electric field is reduced there so that its radial profile becomes hollow. This makes more electric field diffuse into the center, leading to larger runaway production there at the expense of less generation elsewhere which causes the peaking of the runaway current profile.

Simple but quantitative information about the peaking of the current profile is provided by the time evolution of the internal plasma inductance [4], illustrated in figure 18 (left) for 15 MA disruptions with Ar injection, $\tau_{res} = 34$ ms and different primary runaway seeds. After an initial soft increase of l_{int} (approaching to one) during the seed formation phase, a sharp increase is typically observed when the plasma current becomes dominated by the runaway electrons, which constitutes indeed a distinctive feature of the generation of large runaway currents [9] (for the hot-tail seed at $t_0 = 1$ ms, the plasma current is dominated too soon by the runaway current to observe the initial soft increase in l_{int}). Figure 18 (right) shows the time evolution of $q(0)$; initially, when the current decays resistively, $q(0)$ increases. As soon as the runaway electrons are generated and the current profile peaks in the plasma center, $q(0)$ starts to fall to values close to one. The final value of $q(0)$, when the full runaway beam is formed, is determined by the plasma internal inductance, l_{int}, as well as by the runaway current, I_r.

The internal inductance of the runaway beam at 100 ms is shown as a function of τ_{res} in figure 19. For the Compton and tritium seeds, the beam inductance is typically ~2. The analysis in [9] found that the peaking of the runaway current during the disruption, as quantified by the internal inductance, l_{int}, decreases with the runaway plateau current fraction, I_r/I_0, and is also dependent on the peaking of the initial seed current (increasing moderately with the internal inductance of the seed current, l_{int}^{seed}). Hence, in figure 19, the large values of l_{int} observed for the hot-tail seed at $t_0 = 3$ ms are due to the strong initial peaking of the runaway seed (see figure 10) together with the relatively low resulting runaway current fraction, I_r/I_0. For the case of the hot-tail seed at $t_0 = 1$ ms, even if the peaking of the initial seed is also strong, l_{int} becomes lower due to the significantly larger runaway production and larger I_r/I_0.

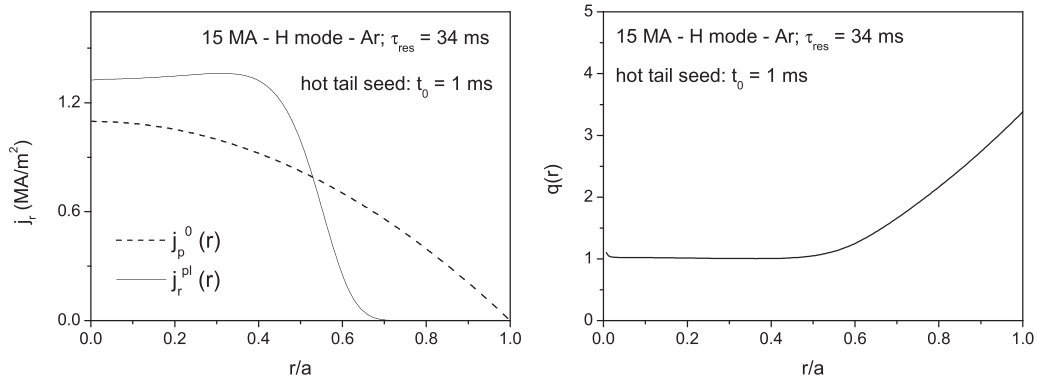

Figure 17. Plateau current density (left) and safety factor (right) profiles for a 15 MA ITER disruption with Ar injection, $\tau_{res} = 34$ ms and hot-tail runaway seed with $t_0 = 1$ ms. The dashed line in the left figure corresponds to the initial current density profile.

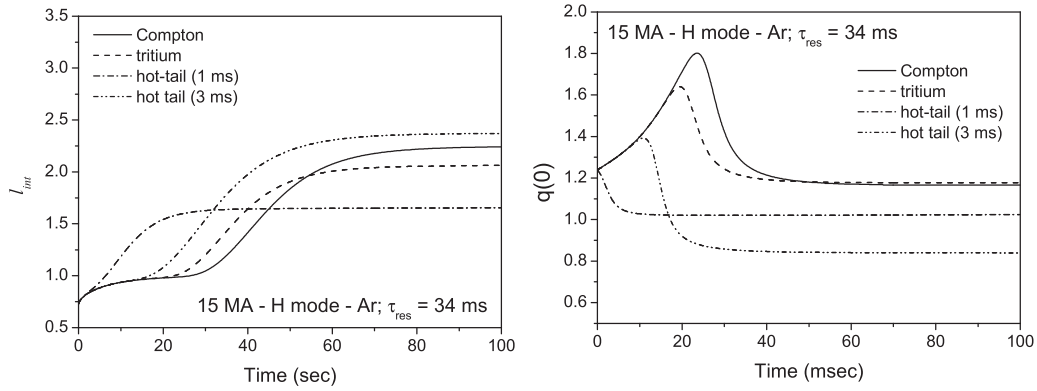

Figure 18. Time evolution of l_{int} (left) and $q(0)$ (right) for 15 MA ITER disruptions with Ar injection, $\tau_{res} = 34$ ms and different primary runaway seeds.

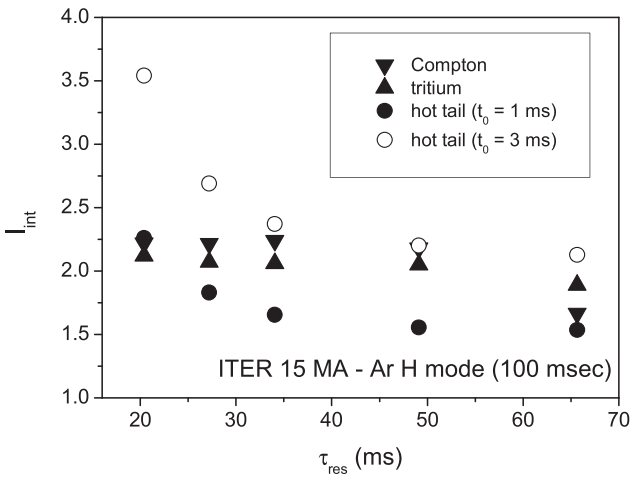

Figure 19. Internal plasma inductance, l_{int}, at 100 ms versus τ_{res} for 15 MA ITER disruptions with Ar injection and different primary runaway seeds.

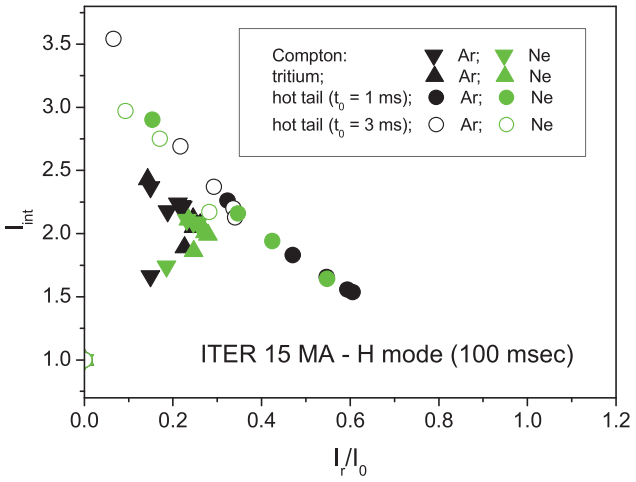

Figure 20. Internal plasma inductance, l_{int}, at 100 ms versus runaway current fraction, I_r/I_0, for 15 MA ITER disruptions with Ar and Ne injection, $\tau_{res} \sim 22$–66 ms and different primary runaway seeds.

This is better illustrated in figure 20, which shows the predicted internal inductance at 100 ms as a function of the runaway current fraction, I_r/I_0, for 15 MA ITER disruptions with Ar and Ne injection, $\tau_{res} \sim 22$–66 ms and different primary runaway seeds. In agreement with the findings in [9], there is a clear trend in l_{int} to decrease with I_r/I_0 and, for a given I_r/I_0, l_{int} is larger for the hot-tail seeds (in comparison with the Compton and tritium seeds) due the stronger peaking of the initial seed profile.

In figure 21, $q(0)$ at 100 ms is plotted as a function I_r/I_0 for the same disruption scenarios that in figure 20. The values of $q(0)$ are always close to one, being larger for the Compton and tritium seeds ($\sim$1.2) than for the hot-tail seed ($\sim$0.7–1) due to the larger peaking of the current density profile in the later case. For the hot-tail seed, as a result of the decrease of l_{int} when the runaway current fraction increases, a trend is observed in $q(0)$ to increase with I_r/I_0.

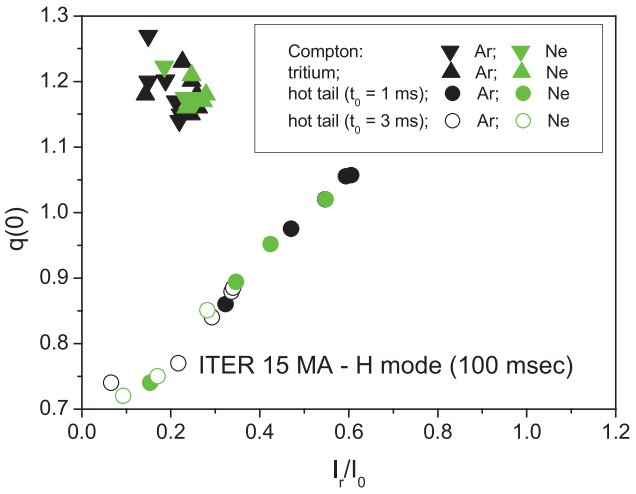

Figure 21. $q(0)$ at 100 ms versus runaway current fraction, I_r/I_0, for the same disruption scenarios as in figure 20.

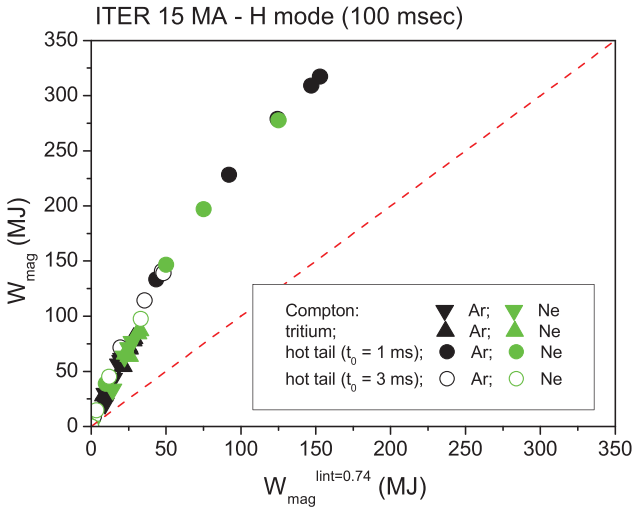

Figure 22. Magnetic energy, W_{mag}, of the runaway beam at 100 ms for 15 MA ITER disruptions with Ar and Ne injection ($\tau_{res} \sim 22$–66 ms) versus W_{mag} estimated by assuming that no current profile peaking has occurred during the disruption current quench ($l_{int} = l^0_{int} \sim 0.7$).

The peaking of the runaway current density profile can have some important consequences from the point of view of the evaluation of the energy that can be deposited by runaway electrons onto the PFCs during disruptions. In first place, the internal magnetic energy of the runaway beam, for a given runaway current, I_r, is given by

$$W_{mag} = \frac{1}{2}\frac{\mu_0 R_0\, l_{int}}{2} I_r^2, \qquad (34)$$

which can be substantially larger (see figure 22) when compared with the values expected for constant l_{int} for the same I_r.

Secondly, the strong peaking of the runaway current profile during the disruption current quench can lead to the formation of MHD unstable runaway beams [13]. Figure 23 shows, for 15 MA disruptions with $\tau_{res} \sim 34$ ms with different runaway seeds, the plasma trajectories in $l_{int} - q_a$ space ($q_a \equiv q(a)$, as explained at the beginning of this section, corresponds to the cylindrical q at $r = a$ corrected by a geometrical factor in order to get a more realistic estimate of the edge q so that, for 15 MA plasma current, $q(r = a) \sim 3$). The high-l_{int} empirical stability boundary (red line) is also indicated in the figure [42]. Figure 23 suggests that, in most of the cases, the runaway beam may become MHD unstable. This is better illustrated in figure 24 which shows, for disruptions at 15 MA, Ar and Ne injection, and $\tau_{res} = 22$–66 ms, the plasma parameters at 100 ms in the $l_{int} - q_a$ space. The Compton and tritium seed cases cluster close to the high—l_{int} boundary, while the hot-tail seed cases, with a substantially larger l_{int}, can lie well above this boundary.

It should be noted that by the time (t_{stab}) at which the plasma crosses the stability boundary in $l_{int} - q_a$ space, the runaway beam is almost fully formed and its current and energy values do not significantly differ from those at 100 ms. This time, t_{stab}, is plotted in figure 25 for the same disruption scenarios as in figure 24 as a function of I_r, suggesting that the plasma can become MHD unstable, particularly for the largest runaway currents, well before the expected time for the vertical instability growth in ITER (~100 ms) [14].

3.2. Disruption termination

3.2.1. General considerations. To study the termination of the runaway plasmas we use the 1D model (equations (2) and (3)) for the analysis of the conversion of magnetic into runaway kinetic energy and for the evaluation of the runaway power loads on the PFCs. The runaway electron losses, neglected during the disruption current quench ($\tau_L \to \infty$) in equation (3), are assumed to start at the time for the vertical instability growth (~100 ms).

0D modelling of the termination phase of runaway plasmas during the disruption has shown to account for the observations in present devices [6]. The efficiency of conversion of the runaway plasma magnetic energy into runaway kinetic energy has been found to be determined to a great extent by the ratio of the characteristic runaway loss time, τ_L, to the resistive time of the residual plasma after the disruption, τ_{res}, increasing with τ_L/τ_{res}. For fast enough terminations (τ_L low), the conversion of magnetic energy into runaway kinetic energy is mainly determined by the acceleration of the runaway electrons due to the induced electric field during current termination and the role played by the avalanche generation of runaway electrons is small ($\tau_L \ll \tau_s$) [6]. Secondary runaway generation by avalanche during runaway terminations leads to an increase in the conversion of magnetic energy into runaway kinetic energy but this is only sizeable for high runaway currents and for long durations of the termination. Extrapolations for ITER have shown that, for long current quench times, when large runaway current beams can be formed and, if the runaway loss time during termination is slow enough ($\tau_L > 1$ ms), the generation of runaways by the avalanche mechanism can increase substantially the energy deposited by the runaways onto the PFCs up to a few hundreds of MJs [6, 38].

The amount of energy deposited onto the PFCs by runaway electrons during current termination could increase compared to 0D estimates due to the following effects:

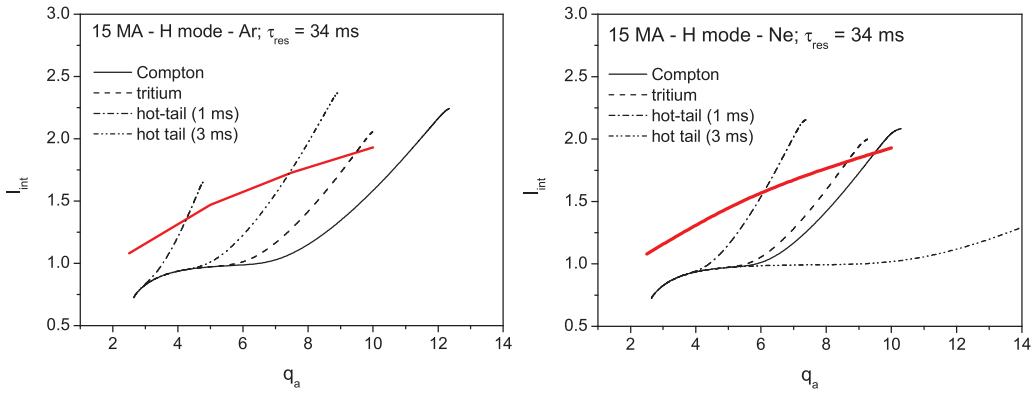

Figure 23. Plasma trajectories in $l_{\rm int} - q_a$ space for 15 MA disruptions with $\tau_{\rm res} \sim 34$ ms and different runaway seeds. The high-$l_{\rm int}$ empirical stability boundary (red line) is indicated.

1. Energy conversion due to acceleration of the runaway electrons by the induced electric field during the termination phase of the disruption is determined by the ratio of the characteristic runaway loss time, $\tau_{\rm L}$, to the plasma resistive time, $\tau_{\rm res}$, increasing with $\tau_{\rm L}/\tau_{\rm res}$ [6]. The peaking of the current density profile leads to a decrease of the effective plasma minor radius (inside which most of the runaway population is located), $a_{\rm eff}$, and, as a consequence, to a lower resistive time,

$$\tau_{\rm res} \equiv \frac{L}{R_{\rm p}} \approx \frac{L a_{\rm eff}^2}{2R_0\,\eta}, \tag{35}$$

which would result in a larger conversion of magnetic into runaway kinetic energy by acceleration of the runaway electrons during current termination when compared with 0D model (flat current density profile) predictions with the same $\tau_{\rm L}$. This is illustrated in figure 26, which shows the amount of magnetic energy that would be converted into runaway kinetic energy,

$$\Delta W_{\rm run} = \int_{\rm termination} {\rm d}t' \int j_{\rm r}\,(E_\parallel - E_{\rm R})\,{\rm d}v, \tag{36}$$

normalized to the initial internal magnetic energy, $W^0_{\rm mag}$, as a function of $\tau_{\rm L}$ during the termination of a runaway beam of 10 MA and 20 MJ (corresponding to an average runaway energy $\sim$15 MeV), for different initial runaway current profile shapes ($l^0_{\rm int} = 0.74$, 1.5 and 2) and assuming that no avalanche generation of runaway electrons during current termination is occurring (i.e. conversion of magnetic into runaway energy is only due to acceleration of the runaway electrons by the induced electric field). The plasma conditions correspond to those of 15 MA Ar disruptions with $\tau_{\rm res} \sim 34$ ms, and the timescale for the runaway losses is in the range $\tau_{\rm L} = 0.1$–10 ms, consistent with the observations in present devices [6]. The dashed line in the figure corresponds to the 0D model predictions [6],

$$\frac{\Delta W_{\rm run}}{W^0_{\rm mag}} \approx \frac{1}{1 + (\tau_{\rm res}/\tau_{\rm L})}. \tag{37}$$

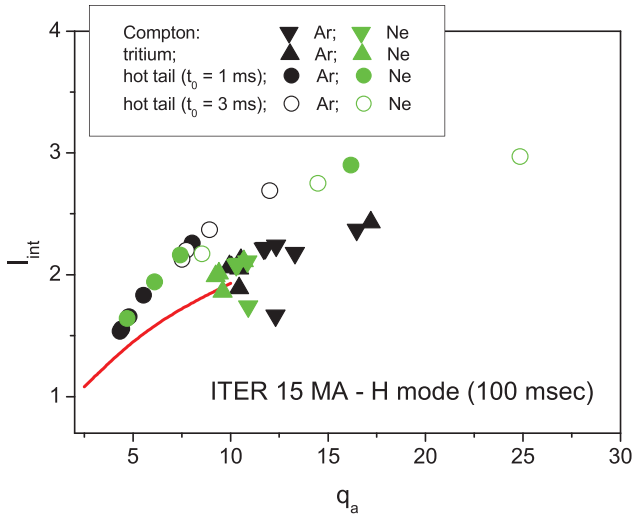

Figure 24. Plasma parameters at 100 ms in $l_{\rm int} - q_a$ space for 15 MA ITER disruptions, Ar and Ne injection, and $\tau_{\rm res} = 22$–66 ms. The high-$l_{\rm int}$ empirical stability boundary (red line) is also indicated.

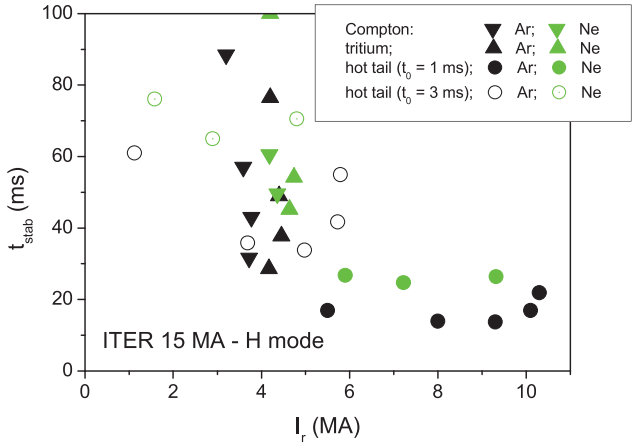

Figure 25. Time, $t_{\rm stab}$, at which the plasma crosses the stability boundary in $l_{\rm int} - q_a$ space as a function of $I_{\rm r}$ for the same disruption scenarios as in figure 24.

2. Energy conversion due to runaway avalanche increases significantly for initially peaked (at the start of the termination phase) runaway current density profiles. This is

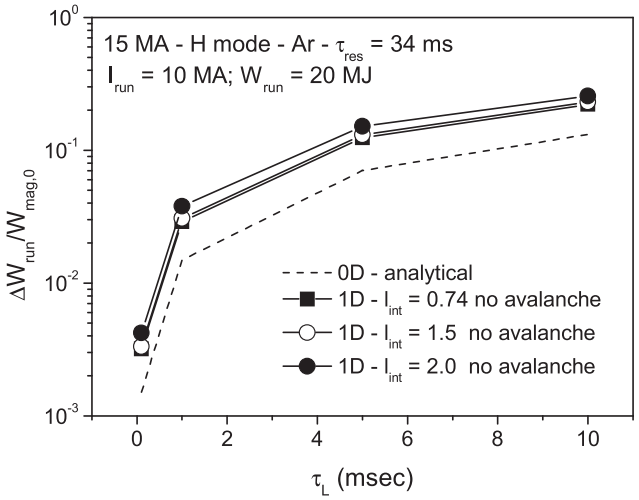

Figure 26. $\Delta W_{\rm run}/W^0_{\rm mag}$ versus $\tau_{\rm L}$ for the termination of a 10 MA/20 MJ runaway beam, and parameters corresponding to 15 MA disruptions with Ar and for $\tau_{\rm res} \sim 34$ ms. The predictions for three different initial runaway current density profiles ($l_{\rm int} = 0.74$, 1.5 and 2) and the 0D model are compared. No runaway avalanche is assumed during the termination of the runaway plateau beam.

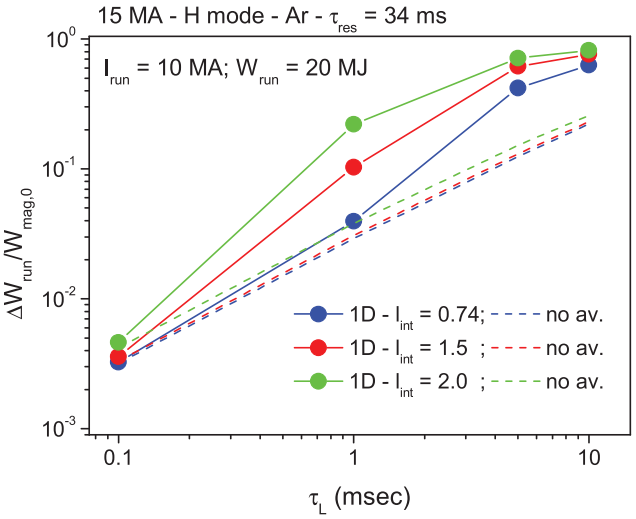

Figure 27. $\Delta W_{\rm run}/W^0_{\rm mag}$ versus $\tau_{\rm L}$ for the termination of a 10 MA/20 MJ runaway beam with $l_{\rm int} = 0.74$, 1.5 and 2. The secondary generation of runaway electrons during the termination of the runaway beam is taken into account. The predictions were made assuming no runaway avalanche (dashed lines) is also included for comparison. Plasma parameters are the same as in figure 26.

shown in figure 27, which compares, for the termination of a 10 MA/20 MJ runaway current, the energy conversion efficiency, $\Delta W_{\rm run}/W^0_{\rm mag}$, for $l^0_{\rm int} = 0.74$, 1.5 and 2, taking into account the secondary generation of runaway electrons during the current termination phase. The calculations performed neglecting the effect of avalanche (dashed lines) are also included, for illustration. The plasma conditions are the same that in figure 26. It is clear from figure 27 that avalanche effects on the conversion of magnetic energy increase substantially with the initial peaking of the current profile and can be already significant for relatively fast terminations ($\tau_{\rm L} \sim 1$ ms). The peaking of the runaway current profile increases the current density in the center and, therefore, the avalanche multiplication in the central region of the plasma. This is supported by the calculated time evolution of $l_{\rm int}$ during current termination, as illustrated in figure 28 for the termination of a 10 MA/20 MJ runaway beam with $l^0_{\rm int} = 2$ and residual plasma conditions corresponding to a 15 MA Ne mitigated disruption with $\tau_{\rm res} \sim 34$ ms. Figure 28 (top) compares the predicted energy conversion efficiency with and without avalanche runaway generation, showing a similar behavior to that illustrated in figure 27. Figure 28 (bottom) shows the time evolution of $l_{\rm int}$ during the termination phase of the disruption for different values of $\tau_{\rm L}$ including (right) and without (left) runaway avalanche. The avalanche mechanism increases the runaway population in the plasma center and can lead, for the slowest terminations, for which the avalanche is largest, to a significant transient increase of $l_{\rm int}$ during termination of the runaway plasma.

3.2.2. Self-consistent modeling of runaway formation and termination. In this section we describe a self-consistent analysis of the disruption current quench and runaway beam termination phases in ITER. In this analysis the runaway current formed during the current quench phase is then utilized to study its termination during the final phase of the disruption. The third term in equation (3), considered negligible during the runaway beam formation ($\tau_{\rm L} \to \infty$), is assumed to increase ($\tau_{\rm L}$ finite), leading to runaway electron losses during the disruption termination phase, which begins at the expected time for the vertical instability growth in ITER ($\sim$100 ms).

An example of these modelling studies is shown in figure 29, which shows the runaway formation and termination phases of a 15 MA H-mode disruption. At 100 ms, the runaway current (figure 29 (left)) is $\sim$9 MA and the kinetic energy of the runaway beam (figure 29 (right)) $\sim$21 MJ. Then, the termination phase starts ($\tau_{\rm L} = 5$ ms) and the plasma current and the runaway electrons are lost. The loss of the current gives rise to an induced electric field and an ohmic current (up to $\sim$3 MA), and magnetic energy is converted into runaway kinetic energy. The total energy deposited by the runaway electrons on the PFCs is given by

$$W_{\rm run} = W^0_{\rm run} + \Delta W_{\rm run}, \qquad (38)$$

where $W^0_{\rm run}$ is the runaway kinetic energy at the start of the termination phase ($\sim$21 MJ) and $\Delta W_{\rm run}$ is the amount of magnetic energy converted into runaway kinetic energy during the termination of the current, given by equation (36), which in the case of figure 29 amounts to $\Delta W_{\rm run} \sim 172$ MJ. The total energy deposited by the runaway electrons on the PFCs is $\sim$193 MJ.

In the following, we present an analysis of the magnetic to kinetic energy conversion in ITER disruption terminations focusing in the conditions potentially leading to the largest loads on PFCs, 15 MA D-T H-mode disruptions, and comparing the results for Ar and Ne injection for thermal

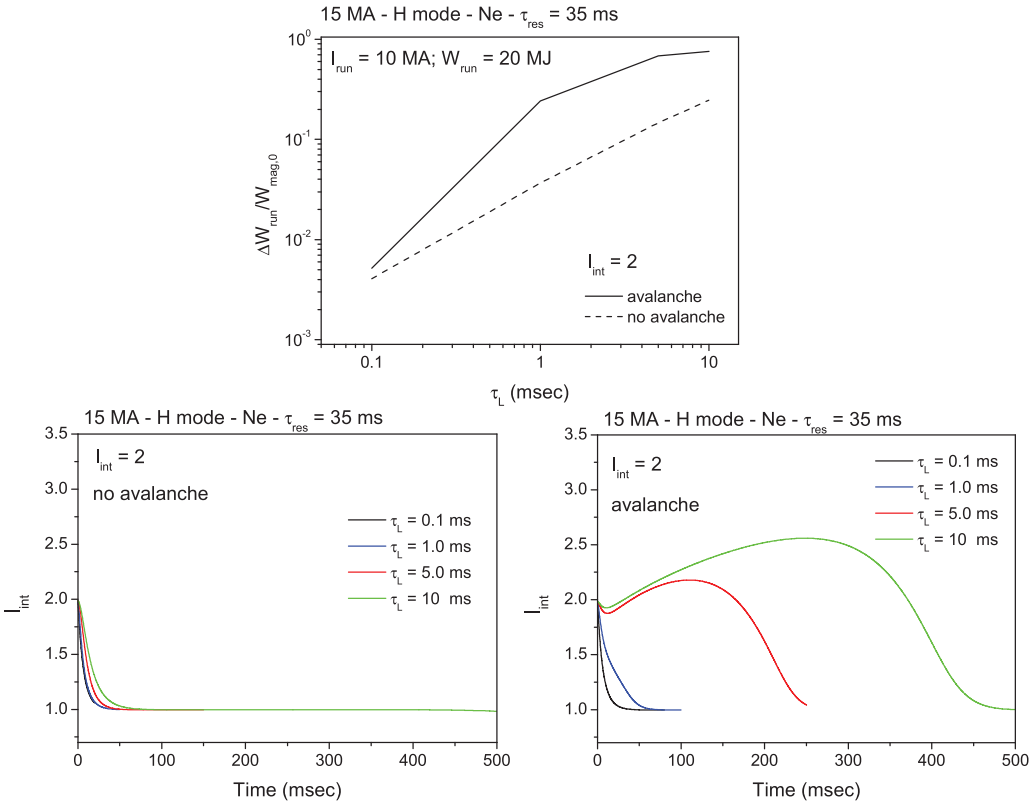

Figure 28. For the termination of a 10 MA/20 MJ runaway current, with $l_{\rm int} = 2$ and plasma conditions as those of 15 MA Ne mitigated disruptions with $\tau_{\rm res} \sim 35$ ms: top: $\Delta W_{\rm run}/W^0_{\rm mag}$ versus $\tau_{\rm L}$. The predictions were made assuming no runaway avalanche (dashed line) is also included; bottom: time evolution of $l_{\rm int}$ during runaway beam termination for different values of $\tau_{\rm L}$ with (right) and without (left) runaway avalanche included.

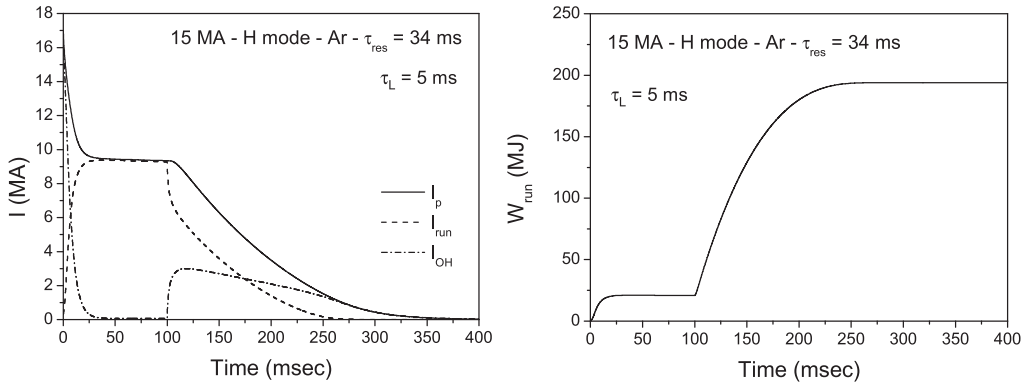

Figure 29. For a 15 MA H-mode disruption with Ar injection and $\tau_{\rm res} = 34$ ms: left: time evolution of the total plasma current, runaway current and ohmic current during the current quench and termination phases of the disruption. The termination phase starts at 100 ms and $\tau_{\rm L} = 5$ ms. Right: time evolution of runaway kinetic energy gain.

quench mitigation. The processes and instabilities that lead to the final loss of the runaway plasma are not well understood and there is a large variability regarding the events that terminate them and in their timescales [4]. The observations in actual devices are based on the emission of hard x-rays or the photoneutron emission produced when the electrons impinge on the plasma facing components [4–6] and can be summarized as:

- the runaway electrons can be lost in a single event or in a series of bursts over a given time interval [4].
- the duration of the runaway loss in the JET, DIII-D and FTU tokamaks ranges typically from 1 to 10 ms, showing no clear correlation with the device size nor with the magnitude of the runaway current [6].
- simulations of the current termination by means of 0D modelling indicate that the observed runaway loss time

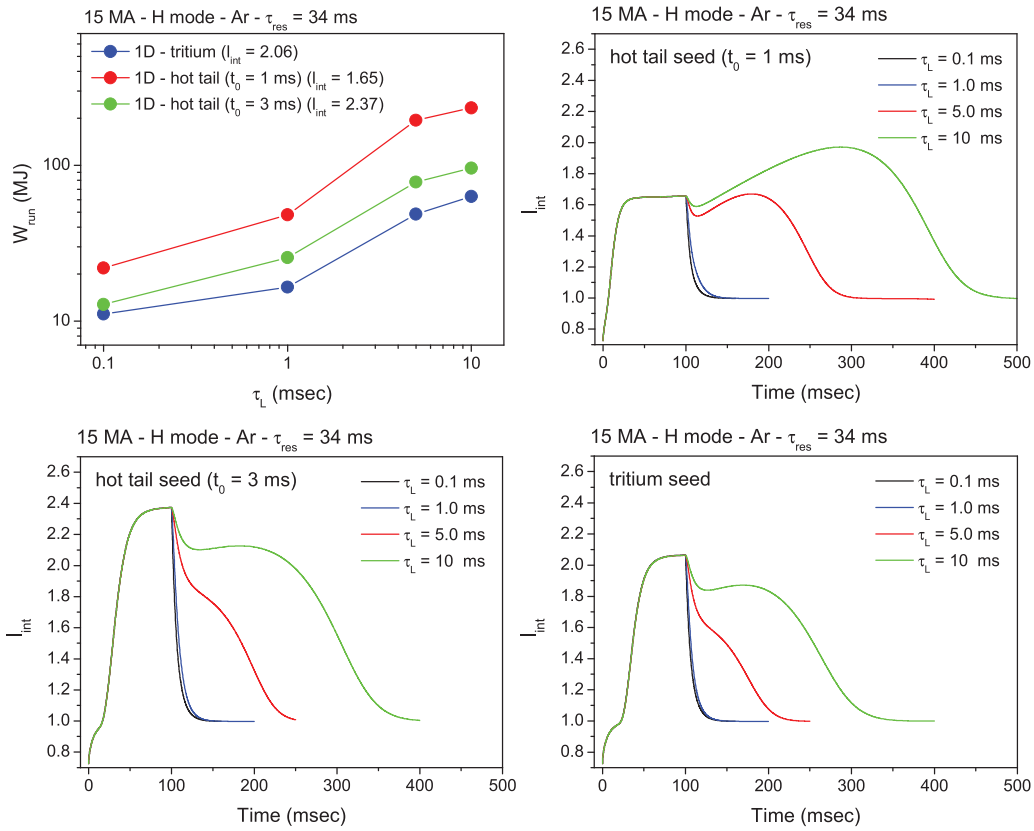

Figure 30. For 15 MA H-mode disruptions, Ar injection and $\tau_{res} = 34$ ms: top left picture: energy deposited by the runaway electrons during the termination phase, W_{run}, versus τ_L for three selected scenarios (the internal inductance, l_{int}, at the start of the termination phase for each scenario is indicated). The top right and the two bottom pictures show, for the three cases, the time evolution of l_{int} during the runaway beam formation and termination phases of the disruption and, in each case, for different values of τ_L.

intervals are consistent with a timescale for the runaway loss $\tau_L \sim 0.1$–5 ms [6].

Given the large uncertainties regarding these runaway termination processes, we carry out our analysis assuming that the runaway electrons are lost in a single event and with a timescale for the runaway losses $\tau_L = 0.1$–10 ms, which has proved to account for the essential features of the termination phase of the current during disruptions in several devices with different sizes and current plateau magnitude [6].

Figure 30 shows the results obtained for 15 MA disruptions with Ar injection, $\tau_{res} \sim 34$ ms and three cases with different runaway seeds showing a large runaway formation during the current quench (see figure 11). Figure 30 (top, left) shows the total energy deposited on PFCs by the runaway electrons during the termination phase, W_{run}, as a function of τ_L for the three selected cases. During fast terminations (small τ_L), the avalanche mechanism has a small effect and the conversion of magnetic into runaway kinetic energy is negligible ($W_{run} \sim W^0_{run}$) [6]. However, when τ_L increases, the secondary runaway generation plays an important role and the energy deposited by the runaways can be as large as a few hundreds of MJs ($\sim 10 \times W^0_{run}$) for the largest τ_L. The other three pictures in figure 30 show the time evolution of the internal inductance for the three cases and, in each of them, for different values of τ_L. The increase of l_{int} during runaway termination is the signature of a strong avalanche in the plasma center which increases with τ_L (slow terminations) and with the amount of runaway current generated during the current quench after the disruption thermal quench.

The results for selected scenarios of 15 MA disruptions with Ne injection and $\tau_{res} \sim 35$ ms (see figure 12) are illustrated in figure 31. Although the runaway current at the start of the termination phase and the effect of avalanche is not as strong as in the Ar case, the total energy deposited by the runaway electrons onto PFCs can be still as large as ~100 MJ ($\sim 9 \times W^0_{run}$).

3.2.3. Non-uniform radial losses. So far, the runaway losses have been assumed radially uniform in the studies presented in this paper, i.e. τ_L has been taken constant across the plasma radius. However, the runaway losses can change radially (that would be the case, for example, of a radius dependent diffusion coefficient, $D_r(r)$, in the case of diffusive losses). Here, we try to get some insight on the effect of a radial variation of the runaway losses on runaway termination assuming τ_L dependent on radius, $\tau_L(r)$. We use a simple description for $\tau_L(r)$, in which it is assumed that τ_L has a constant value, $\tau_{L,1}$, in the inner half of the plasma cross section ($r/a < 0.5$), and a different value, $\tau_{L,2}$, in the outer half ($r/a > 0.5$).

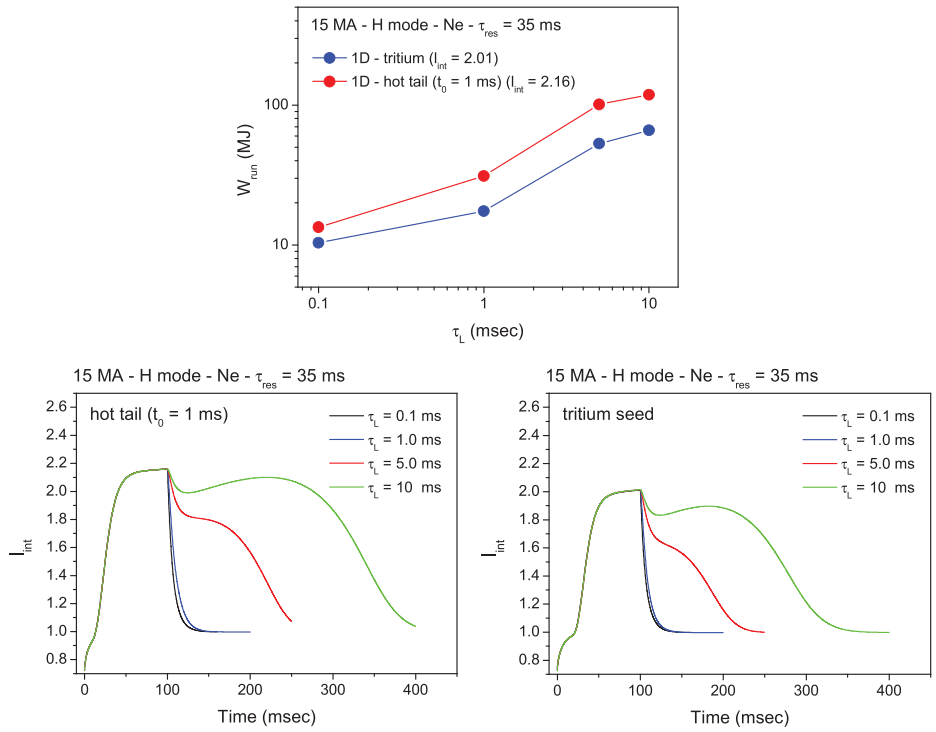

Figure 31. For 15 MA H-mode disruptions and Ne injection: top: $W_{\rm run}$, versus $\tau_{\rm L}$ for selected scenarios; bottom: for the two selected scenarios: time evolution of $l_{\rm int}$ during runaway beam formation and termination for different values of $\tau_{\rm L}$.

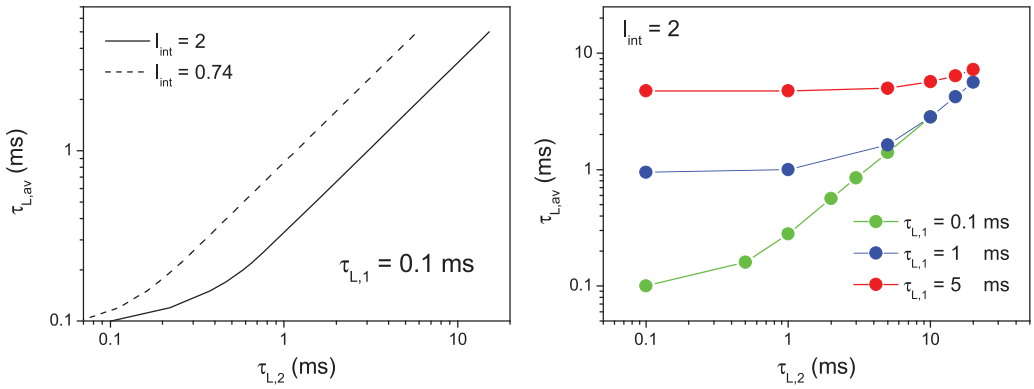

Figure 32. Left: average loss time, $\tau_{\rm L,av}$, versus $\tau_{L,2}$ for $\tau_{L,1} = 0.1$ ms and two different current density profiles: $l_{\rm int} = 2$ (full line), $l_{\rm int} = 0.74$ (dashed line); right: $\tau_{\rm L,av}$ versus $\tau_{L,2}$ for $l_{\rm int} = 2$ and three different values of $\tau_{L,1}$ (=0.1, 1 and 5 ms).

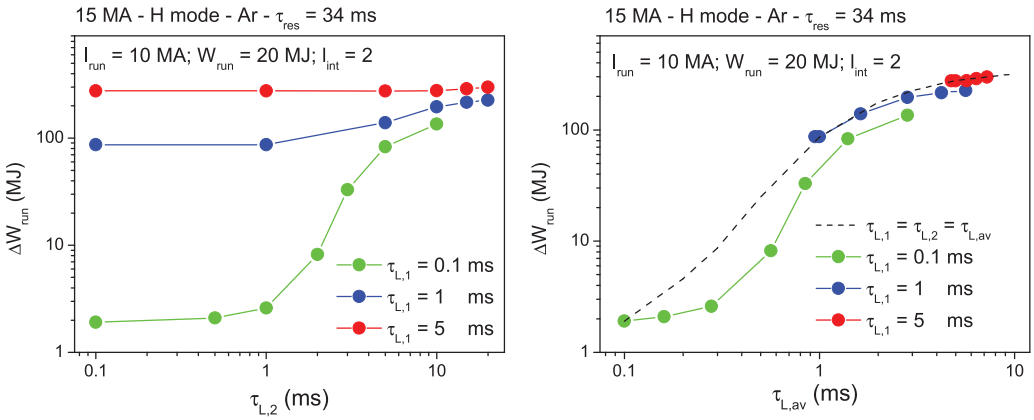

Figure 33. For the termination of a 10 MA/20 MJ runaway beam, $l_{\rm int} = 2$, and parameters corresponding to $\tau_{\rm res} \sim 34$ ms, 15 MA Ar mitigated disruptions: left: $\Delta W_{\rm run}$ versus $\tau_{L,2}$ for three different values of $\tau_{L,1} = 0.1$, 1 and 5 ms; right: $\Delta W_{\rm run}$ versus $\tau_{\rm L,av}$ ($\tau_{L,1} = 0.1$, 1 and 5 ms). The dashed line shows the predictions for a radially constant diffusion time ($\tau_{L,1} = \tau_{L,2} = 0.1$–10 ms).

We introduce for such a profile, $\tau_L(r)$, an equivalent average diffusion time, $\tau_{L,av}$, defined as the diffusion time, constant in radius, that would be required to yield, in the absence of runaway avalanche, a decay of the runaway current with the same time scale as $\tau_L(r)$. It is expected that the conversion of magnetic into runaway kinetic energy during current termination should be determined to a great extent by $\tau_{L,av}$.

If no runaway avalanche is assumed, the runaway current, for the chosen τ_L radial profile, would decay as

$$I_r(t) = I_{01}\, e^{-t/\tau_{L,1}} + I_{02}\, e^{-t/\tau_{L,2}}, \qquad (39)$$

where

$$I_{01} \equiv 2\pi \int_0^{a/2} r\, j_r^0(r)\, dr; \quad I_{02} \equiv 2\pi \int_{a/2}^{a} r\, j_r^0(r)\, dr \qquad (40)$$

($j_r^0(r)$ is the runaway current density profile at the start of the termination phase).

Thus, the equivalent average diffusion time is strongly dependent on the initial runaway current profile, $j_r^0(r)$. This is shown in figure 32 (left) where, assuming $\tau_{L,1} = 0.1$ ms in the plasma center, $\tau_{L,av}$ is plotted as a function of $\tau_{L,2}$ for two different initial runaway current density profiles ($l_{int} = 0.74$ and 2), with the parametrization $j_r^0(r) = j_0\,[1 - (r^2/a^2)]^\nu$. Peaked profiles are more weighted towards the inner region of the plasma (i.e. by $\tau_{L,1}$) and thus, for the same value of $\tau_{L,2}$, the resulting $\tau_{L,av}$ is closer to $\tau_{L,1}$ for $l_{int} = 2$ than for $l_{int} = 0.74$. As illustrated in figure 32 (right), to increase $\tau_{L,av}$ over $\tau_{L,1}$ for peaked current profiles requires a value of $\tau_{L,2}$ in the outer plasma region substantially larger than that of $\tau_{L,1}$. For $\tau_{L,2} < \tau_{L,1}$, the value of $\tau_{L,av}$ is always close to $\tau_{L,1}$.

Due to the fact that the runaway beams generated during the disruption current quench are typically peaked in the plasma center, $\tau_{L,av}$, and, hence, the amount of energy converted into runaway electron kinetic energy during current termination, ΔW_{run}, is dominated by the runaway losses in the central region of the plasma unless $\tau_{L,2}$ is much larger than $\tau_{L,1}$. Hence, figure 33 (left) shows, for the termination of a 10 MA/20 MJ runaway beam, $l_{int} = 2$, and parameters corresponding to $\tau_{res} = 34$ ms of 15 MA Ar mitigated disruptions, ΔW_{run} as a function of $\tau_{L,2}$ (0.1 − 10 ms) for three different values of $\tau_{L,1}$ (= 0.1, 1 and 5 ms). ΔW_{run} is initially determined by $\tau_{L,1}$ and, only when $\tau_{L,2}$ is significantly larger than $\tau_{L,1}$, the average diffusion time, $\tau_{L,av}$ and ΔW_{run} increase. In figure 33 (right), for the same cases ($\tau_{L,1} = 0.1$, 1 and 5 ms), the calculated ΔW_{run} is shown as a function of the average diffusion time, $\tau_{L,av}$, together with the modelling results for a radially constant diffusion time. These results support that ΔW_{run} can be determined to a large extent by evaluating $\tau_{L,av}$ without the need to include detailed features of the radial profile of the runaway loss time $\tau_L(r)$.

3.3. Effect of gas mixtures on the formation and termination of runaway beams in ITER

The analysis described in sections 3.1 and 3.2 has shown that mitigated disruptions by Ar or Ne injection in ITER can lead

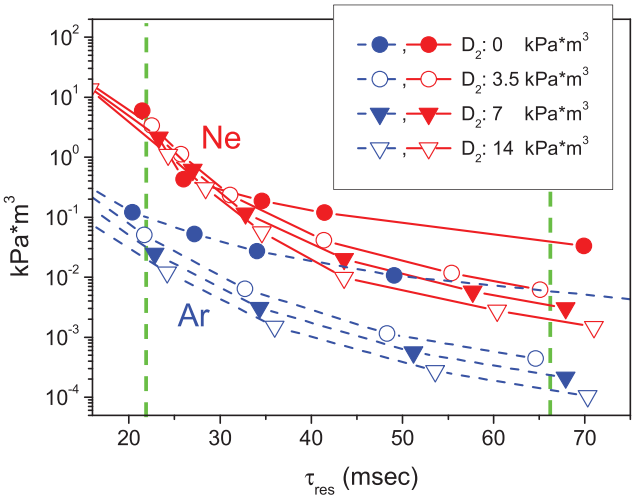

Figure 34. For 15 MA H-mode ITER mitigated disruptions, with Ar + D (blue lines and symbols) and Ne + D (red lines and symbols) gas injection: number of injected impurity atoms (assuming 100% assimilation efficiency) versus τ_{res}. The vertical green dashed lines indicate the range of τ_{res} values leading to acceptable forces onto the vessel and in-vessel components in ITER.

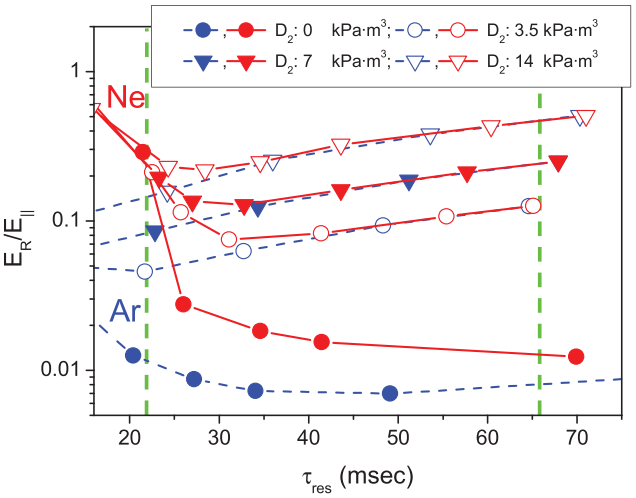

Figure 35. For 15 MA H-mode ITER mitigated disruptions, with Ar + D (blue lines and symbols) and Ne + D (red lines and symbols) gas injection: $E_R/E_\parallel$ ($E_\parallel$ is the electric field at the start of the current quench) versus τ_{res}. The vertical green dashed lines indicate the range of τ_{res} values leading to acceptable forces onto the vessel and in-vessel components in ITER.

to significant runaway current formation, particularly for disruptions with large plasma current and long initial current quenches. In these conditions, if the runaway losses are slow in the runaway termination phase, a strong conversion of magnetic into runaway kinetic energy can take place, mainly due to the avalanche mechanism. This increases substantially the energy deposited by the runaways onto the PFCs which can potentially reach values up to a few hundreds of MJs. In this section we investigate how disruption mitigation can be optimized by the injection of gas mixtures (Ar + D or Ne + D). Deuterium does not radiate significantly so that mixed impurity (Ar or Ne) + deuterium injection allows the

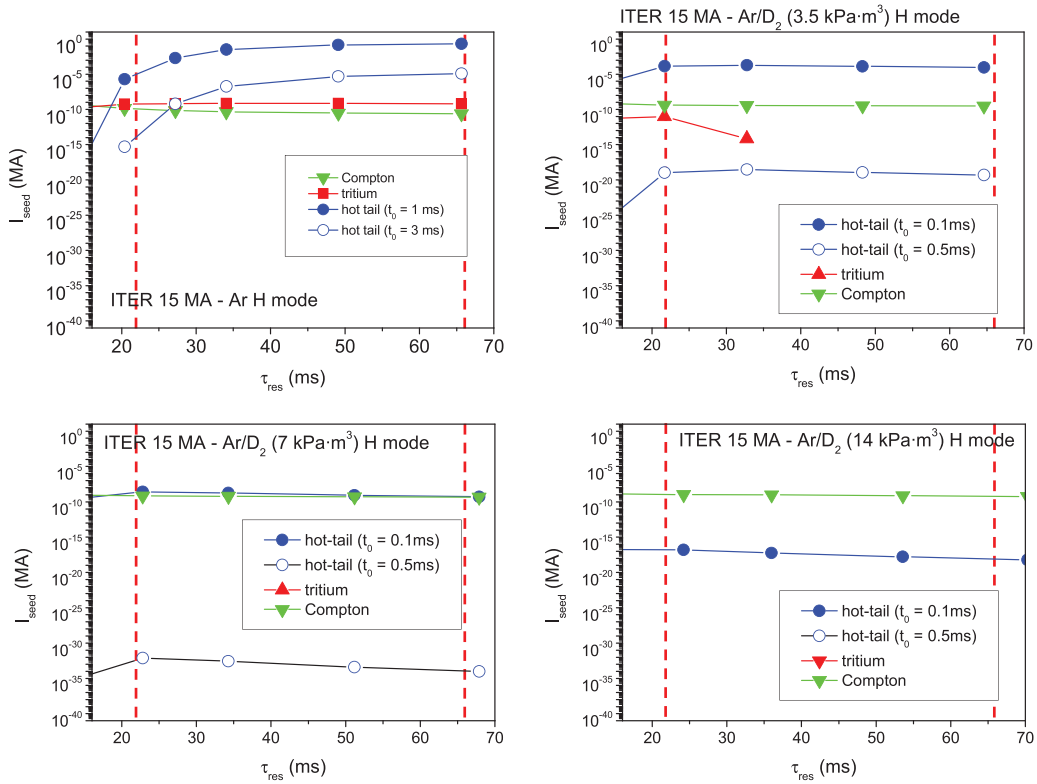

Figure 36. Predicted runaway seed current versus current quench time for 15 MA H-mode disruptions with Ar + D gas injection (amount of injected *D*: 0, 3.5, 7 and 14 kPa · m^3).

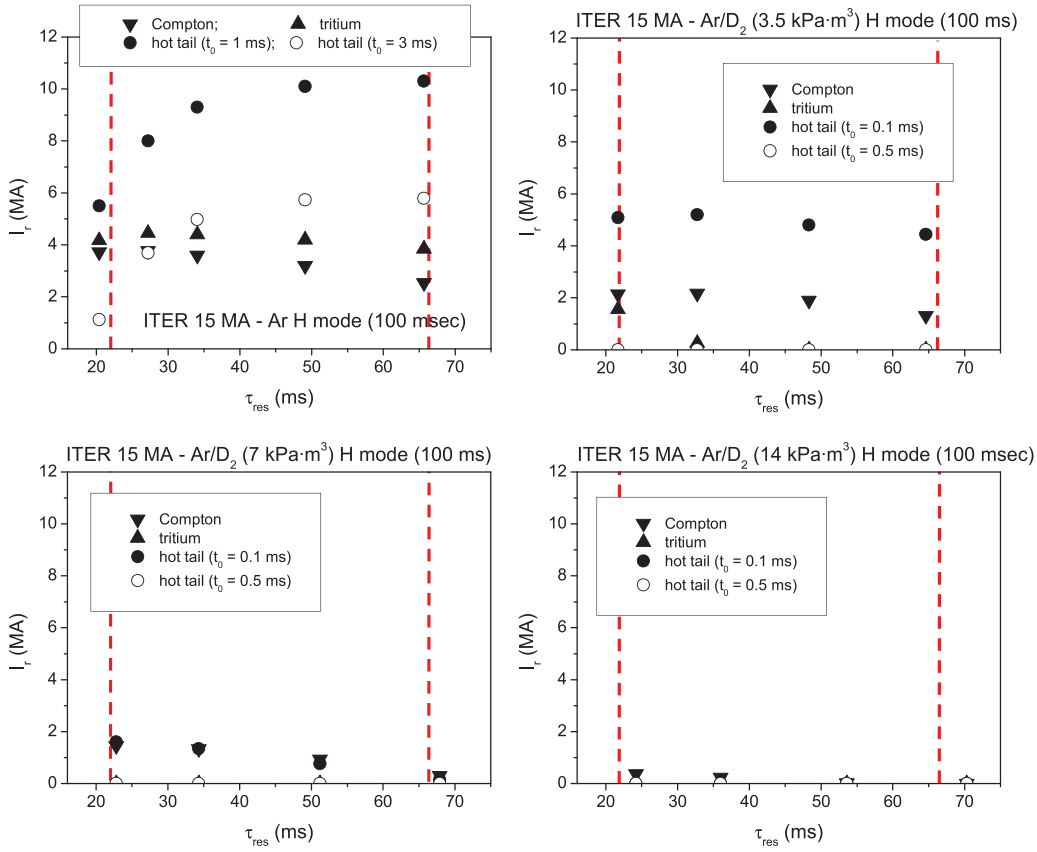

Figure 37. Runaway current at 100 ms versus current quench time for 15 MA H-mode disruptions with Ar + D gas injection. Each frame corresponds to a different amount of *D* (0, 3.5, 7 and 14 kPa · m^3).

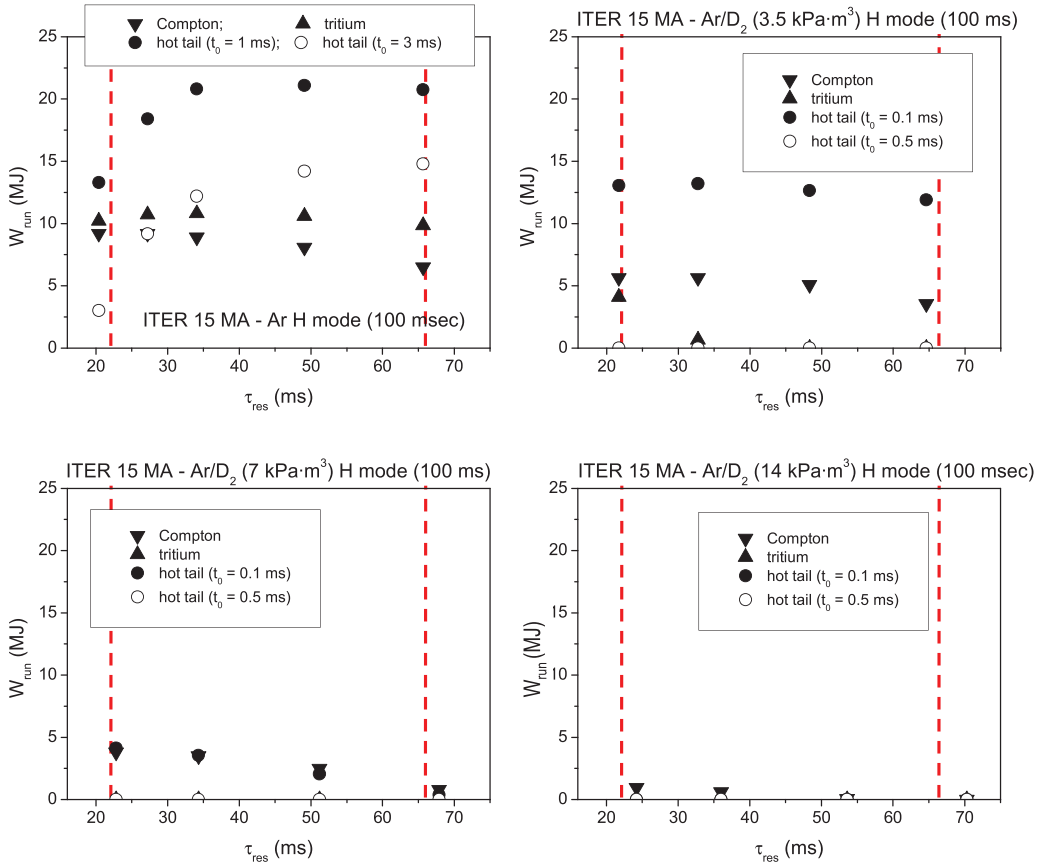

Figure 38. Runaway beam energy at 100 ms versus τ_{res} for the scenarios of figure 37.

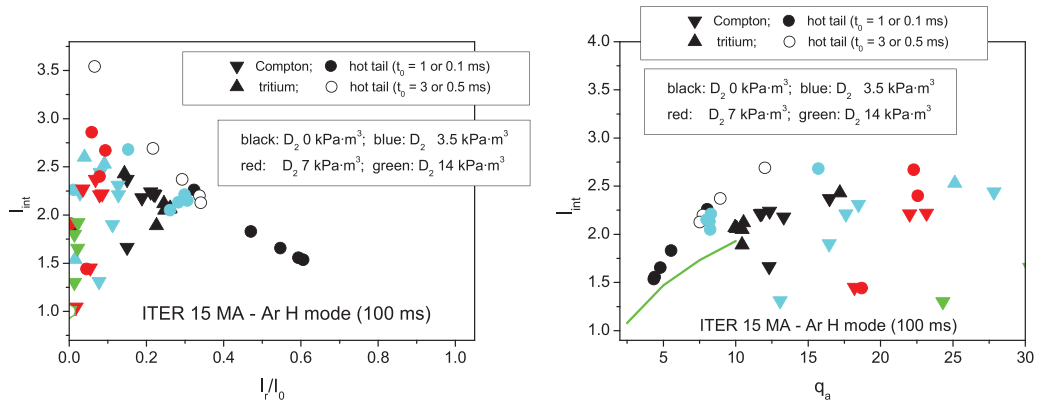

Figure 39. Internal plasma inductance, l_{int}, at 100 ms versus runaway current fraction, I_r/I_0, (left) and q_a (right) for 15 MA ITER disruptions with Ar + D gas injection (amount of injected D: 0, 3.5, 7 and 14 kPa · m^3). The high-l_{int} empirical stability boundary (green line) is also indicated.

achievement of disruption mitigation with similar current quench times to Ar and Ne injection alone but with increased plasma density and collisionality due to presence of the deuterium.

As in section 3.2, we present the results obtained in our studies only for 15 MA D-T H-mode disruptions. Pure Ar or Ne injection is compared with the injection of gas mixtures with three different levels of assimilated deuterium: ∼ 3.5, 7 and 14 kPa · m^3, corresponding to $n_{D_2} = 1, 2$ and 4×10^{21} m^{-3}, respectively (the equivalence between kPa · m^3 and density is set assuming a typical volume ∼830 m^3). Figure 34 compares for Ar (blue lines and symbols) and Ne (red lines and symbols) and, as a function of the current quench time, the amount of impurity atoms that needs to be injected. Due to the injection of D, for the same τ_{res} (∼ T_e), the number of injected impurity atoms, estimated from

$$\eta\, j_{OH}^2 = (n_H + n_D + < Z > \cdot n_z)\, n_z\, L_{imp}, \qquad (41)$$

decreases (n_H is the pre-disruption deuterium + tritium density and n_D the deuterium density). Nevertheless, for Ne and the shortest current quenches ($\tau_{res} < 30$ ms), the amount of impurities is still significant and the results do not differ from the case of pure Ne injection.

The results for $E_R/E_\parallel$ ($E_\parallel$ is the electric field at the start of the current quench) are compared in figure 35. Due to the lower Ne radiation at low T_e, for fast current quenches, $E_R/E_\parallel$ is much larger for Ne than for Ar. Moreover, for Ar, $E_R/E_\parallel$ always increases with the amount of deuterium, while for Ne and the shortest τ_{res}, it is largely insensitive to the deuterium injected because of the large neon density. For long current quenches and D injection, the plasma collisionality, dominated by deuterium, tends to be the same for both, Ar and Ne, resulting in the same $E_R/E_\parallel$ for both impurities.

The injection of deuterium, increasing the plasma collisionality, has an effect on both, the primary runaway sources and the multiplication by avalanche of the runaway seed during the disruption current quench. This is illustrated in figures 36–38 for Ar + D injection. Each frame in every figure corresponds to a different amount of injected D. Figure 36 shows the estimated runaway seed currents. Except for the Compton scattering seed, all the primary runaway sources are very efficiently controlled by D injection and, even the hot-tail runaway generation of very fast thermal quenches (as small as $t_0 = 0.1$ ms exponential decay) can be efficiently reduced when a sufficient large amount of deuterium is injected. The predicted runaway currents and runaway beam energies at 100 ms are shown in figures 37 and 38, respectively. The injection of D is very effective in controlling the runaway beam. Even for the Compton scattering seed, for which the effect of deuterium is smaller, the generation of runaway electrons by the avalanche mechanism can be efficiently controlled by injection of deuterium with an amount larger than ~ 7 kPa · m^3.

The internal inductance, l_{int}, at 100 ms for these scenarios with Ar + D injection is shown versus I_r/I_0 and q_a in figure 39 (left and right, respectively). For the same runaway current fraction, a somewhat lower l_{int} and, therefore, a more MHD stable beam configuration is obtained for mixed Ar + D gas injection when compared with pure Ar injection. The resulting magnetic energy at 100 ms is shown in figure 40. The maximum predicted magnetic energy decreases from ~300 MJ with Ar gas injection alone, to ~100 MJ for an amount of assimilated deuterium ~3.5 kPa · m^3, ~10 MJ for ~7 kPa · m^3, to less than 1 MJ for ~14 kPa · m^3.

Figures 41 and 42 show the results of the analysis for the formation and termination of the runaway current for Ar + D injection with 3.5 and 7 kPa · m^3 D_2 injection, respectively, and selected scenarios for which a large runaway formation without D injection is obtained ($\tau_{res} \sim 34$ ms and hot-tail seed with $t_0 = 0.1$ ms). Figures 41 and 42 (left) show the total energy deposited by the runaway electrons onto PFCs during the termination phase, W_{run}, as a function of τ_L and

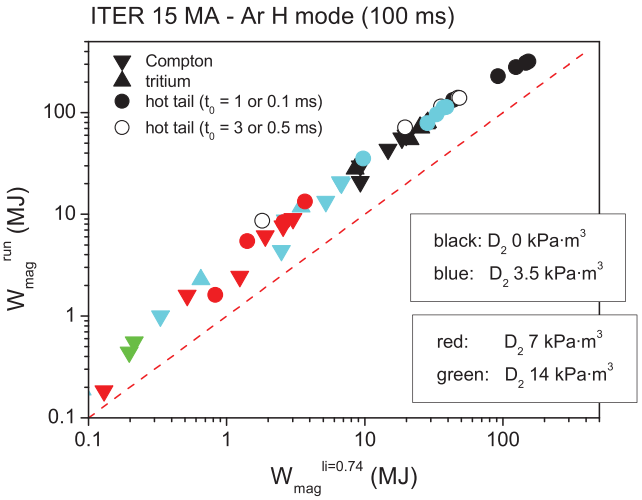

Figure 40. Magnetic energy, W_{mag}, of the runaway beam at 100 ms for 15 MA ITER disruptions with Ar + D gas injection versus W_{mag} estimates made assuming that no current profile peaking has occurred ($l_{int} = l^0_{int} = 0.74$).

the figures 41 and 42 (right) the time evolution of l_{int} for different values of τ_L. The injection of D not only diminishes the runaway current formation as well as the kinetic energy of the runaway beam during the current quench phase, but also reduces the effects associated with the acceleration of the runaway electrons and the secondary runaway generation on the conversion of magnetic into runaway kinetic energy during the termination phase of the runaway beam, the effects increasing with the amount of deuterium injected. Hence, for 3.5 kPa · m^3 deuterium injection, $\tau_{res} \sim 34$ ms and hot-tail runaway seed with $t_0 = 0.1$ ms, the total energy deposited onto PFCs by the runaway electrons during runaway termination decreases down to $W_{run} \sim 6 \times W^0_{run}$ (~80 MJ) in contrast with $W_{run} \sim 10 \times W^0_{run}$ (~220 MJ) for pure Ar injection and hot-tail seed with $t_0 = 1$ ms (figure 30). For 7 kPa · m^3 D_2 injection the total runaway electron energy deposited onto PFCs is further decreased to only $W_{run} \sim 2 \times W^0_{run}$ (~7 MJ). The time evolution of l_{int} shown in these figures clearly illustrates the effectiveness of D injection in controlling the avalanche generation of runaway electrons; already for an amount of D of 7 kPa · m^3, as a result of the reduction of the secondary runaway generation in the plasma center, the current profile does not significantly peak and l_{int} does not increase anymore along the runaway beam termination, but decreases continuously, even for the slowest terminations. It is important to note that the efficiency of the mixed impurity (Ar or Ne) plus deuterium injection in decreasing the amount of energy deposited by the runaway electrons onto PFCs during runaway termination results from two effects: the increase of n_e caused by the added D reduces the runaway seeds and the avalanche amplification in the current quench. In addition the presence of D and the associated density rise also decreases the role played by the runaway avalanche on the conversion of magnetic into runaway kinetic energy during current termination.

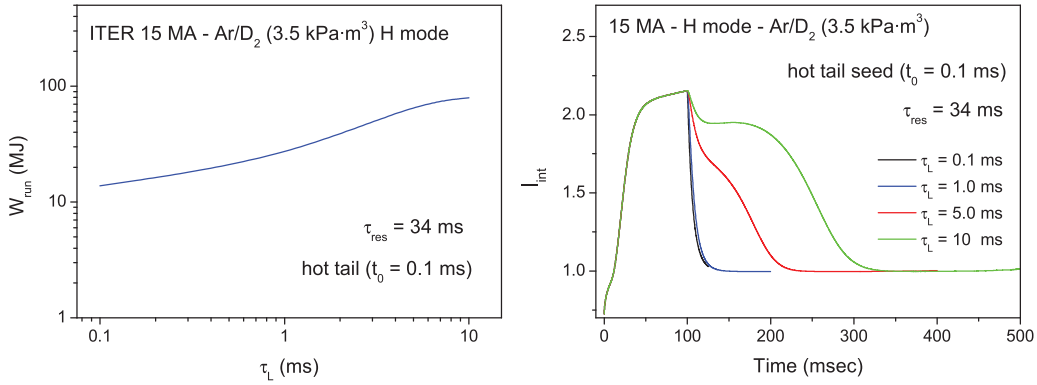

Figure 41. For 15 MA H-mode disruptions with Ar + D injection (3.5 kPa · m^3) and a scenario with a large runaway formation without *D* injection: left: $W_{\rm run}$ versus $\tau_{\rm L}$: right: time evolution of $l_{\rm int}$ for different values of $\tau_{\rm L}$.

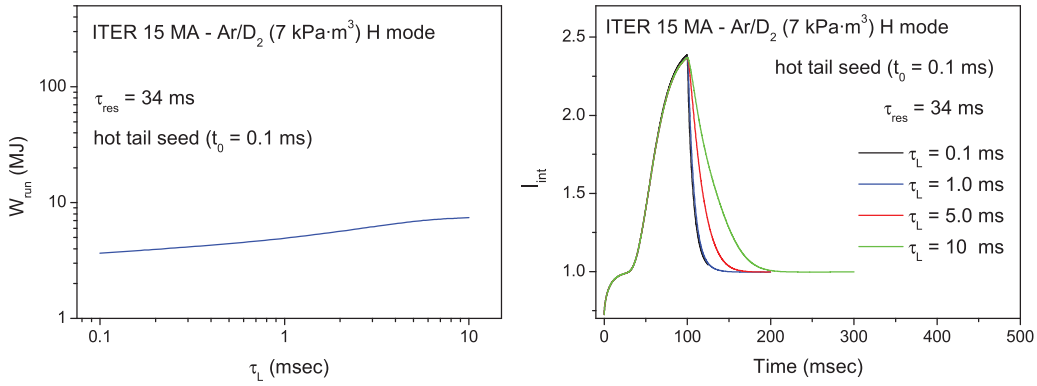

Figure 42. For 15 MA H-mode disruptions and Ar + D injection (7 kPa · m^3) and a scenario with a large runaway formation without *D* injection: left: $W_{\rm run}$ versus $\tau_{\rm L}$: right: time evolution of $l_{\rm int}$ for different values of $\tau_{\rm L}$.

4. Conclusions

In this work, the formation and termination of runaway beams during mitigated disruption scenarios has been investigated for a wide range of plasma conditions in ITER. This has been done by means of a simple one-dimensional disruption model, that includes the essential physical processes: (a) the main runaway generation mechanisms (avalanche and runaway primary sources) expected in ITER, (b) effects associated with the current profile shape during the formation and termination of runaway plasmas, and (c) corrections to the runaway dynamics to account for the collisions of the runaway electrons with partially stripped impurity ions, including the collisions with the free and bound electrons, and the scattering by the full nuclear and the electron-shielded impurity ion charge. Mitigated disruptions by Ar or Ne injection have been considered and their amounts have been varied, leading to current quench times within the range compatible with acceptable forces on the ITER vessel and in-vessel components.

Self-consistent modelling of the runaway beam formation and termination has shown that the collisions of the runaway electrons with impurity ions can play an important role, particularly for Ne injection because of the large amount required due its small radiation efficiency at low $T_{\rm e}$, leading to low runaway production and low energy conversion during current termination for the shortest current quench times ($\sim$22 ms). For long current quench times, due to the lower amount of impurities, larger runaway currents are predicted. For the case of the tritium and Compton seeds typical runaway currents $\sim$4 MA are found. The hot-tail seed, strongly sensitive to the plasma cooling rate, might yield up to $\sim$10 MA runaway current for the longest current quenches and shortest thermal quench durations. The energy deposited by the runaway electrons on the PFCs during the termination phase can increase to a few hundreds of MJs ($\sim 10 \times W^0_{\rm run}$) for the slowest runaway plasma terminations, largest diffusive timescale for runaway loss, mainly due to the avalanche generation of runaway electrons during this phase.

Current profiles shape effects during the formation and termination of the runaway beam have been shown to be important. In first place, the inferred amount of impurities required for a given current quench time is substantially smaller when current profile effects are considered than when 0D analysis is applied [38]. The observed trends in $I_{\rm r}$ and $W_{\rm run}$ are similar to those found by means of a zero-dimensional model of the disruption [38]. For the shortest current quenches, because of the lower amount of required impurities, the resulting runaway currents and beam kinetic energies are larger for the 1D evaluation than in the 0D case. In contrast, for the longest current quenches, for which the impurity density is low, both in the 0D and 1D modelling, the calculated runaway currents and

energies are lower in the 1D calculations as the runaway electrons are mostly generated in the central region of the plasma where, although the electric field is larger than in the 0D model, the available volume is substantially smaller [9].

As predicted in the past [11, 12], and supported by experimental observations [4, 10], the runaway current density profile created during the current quench phase is more peaked than the pre-disruption plasma current. Such a peaking, quantified by the internal inductance, l_{int}, is found to decrease with the runaway current fraction and is also sensitive to the peaking of the initial seed current which, for the same value of I_r/I_0 , can be noticeably larger for the hot-tail seed than for the Compton and tritium seeds. This peaking of the runaway current profile can have important implications as: (a) it increases (for a given runaway current) the magnetic energy of the runaway beam that might be converted into runaway kinetic energy during the termination phase of the disruption; (b) the runaway plasma can be less MHD stable. Indeed, the examination of the plasma trajectories in $l_{\mathrm{int}} - q_a$ space suggests that the runaway beam crosses the high-l_{int} empirical MHD stability boundary before the expected time for the vertical instability growth in ITER, although, by that time, the beam is essentially already formed and has a current similar to that in the plateau phase. This might lead to an early termination of the runaway plasma (before $\sim$100 ms) which is not considered here. The safety factor on axis, $q(0)$, is always close to one (larger than one for the tritium and Compton seed cases, and slightly dropping below one when $I_r/I_0 < 0.5$ for the hot-tail seed) due to the larger current profile peaking. The peaking of the runaway current profile also enhances significantly the role played by the runaway avalanche during runaway current termination, increasing (for a given runaway plateau current at the start of the termination phase) the energy conversion efficiency in comparison with the 0D calculations [6, 38], even for relatively fast terminations ($\tau_L \sim 1$ ms).

Mixed Ar + D or Ne + D injection has been found to be effective in controlling the magnitude of the runaway current after the thermal quench as well as that of the runaway power loads onto the PFCs for an assimilated amount of D of $\sim$14 kPa $\cdot$ m^3. While the amount of injected Ar or Ne provides current quench times within the range for acceptable mechanical loads on the ITER vessel and in-vessel components, the injection of D allows increasing the plasma collisionality without affecting τ_{res}, thus reducing the runaway avalanche at the initial current quench and enhancing runaway energy dissipation. For 7 kPa $\cdot$ m^3 D injection, the amount of energy deposited by the runaway electrons during current termination already decreases to $W_{\mathrm{run}} \sim 2 \times W^0_{\mathrm{run}}$ (less than 10 MJ). For $\sim$14 kPa $\cdot$ m^3 deuterium injection fully prevents the conversion of magnetic into runaway energy during disruption termination and the runaway energy loads are less than 1 MJ for all seed mechanisms and runaway loss times at termination. The injection of deuterium also controls efficiently the primary runaway sources (except for the Compton scattering seed) as well as the avalanche multiplication of the runaway seed during the disruption current quench. Both the reduction of the seeds and the decreased avalanche at the current quench and runaway termination, as a consequence, substantially reduce the conversion of magnetic into runaway kinetic energy during runaway plasma termination.

It must be noted that some potentially important effects, such as the dissipation of runaway electron energy due to synchrotron radiated power, have been neglected in the modelling presented here. Indeed, kinetic simulations [43, 44] have shown that enhanced synchrotron radiation losses associated with the increase in the electron pitch angle due to the collisions of the runaway electrons with impurity ions may be responsible for the runaway energy dissipation experimentally observed when injecting high-Z impurities during the runaway plateau phase of disruptions in DIII-D and Tore Supra [5, 45], constituting one of the most promising mechanisms foreseen for runaway mitigation during disruptions in ITER [46]. The synchrotron radiation losses in plasmas with large enough impurity content reduce the electron energy, increase the value of the critical field for runaway generation and lead to a bump formation in the runaway distribution function [44]. Nevertheless, from the point of view of the analysis in this paper, in which impurity injection has been assumed to occur before the thermal quench, the scenarios for which synchrotron radiation losses could play a major role (short current quenches with large impurity densities) have been found to have low runaway currents by considering the collisional dissipation effects alone. For long current quench conditions, with low impurity content, the synchrotron radiation losses should be low. Therefore, from the point of the identification of the disruption conditions in ITER that can potentially lead to the largest runaway loads onto PFCs, no substantial changes are expected by the inclusion of synchrotron radiation with respect to the analysis presented here.

The modelling approach presented in this paper provides a self-consistent simulation of runaway formation and termination from the thermal quench to the end of the runaway plateau during tokamak disruptions triggered by massive material injection with specific application to ITER. Obviously, such approach requires a significant degree of simplification as many of the individual physics processes (runaway losses during the thermal quench, assimilation of injected material during the thermal quench, MHD instability leading to the final termination of the runaway discharge, etc) involved are very complex and a full self-consistent model that describes all of them is not available or is expected to be available in the near future. This implies that the conclusions of our model are not quantitative enough to provide input to the design of the disruption mitigation system, which is not the purpose of this study. The aim of this study is to identify key factors that drive the formation of runaways in ITER following massive material injection for mitigation of thermal loads and halo currents as well as the consequences of these for the termination of the runaway beams which are formed in a self-consistent way, and to aid to the identification of the most relevant issues for a more detailed modelling and for the design of the ITER disruption mitigation system, among them:

(a) The analysis reported in this paper does not include the disruption thermal quench but assumes given plasma

conditions after the thermal quench. Moreover, only mitigated disruption scenarios are assessed in this work and natural thermal quenches are not considered. The impact of the nature of the thermal quench process (natural thermal quenches or induced during mitigation of thermal loads and halo current [20]) should be addressed in the future.

(b) The impurities have been assumed to be deposited uniformly over the plasma. This provides information about what is the best mitigation approach in terms of the species injected to minimize the runaway production (Ar, Ne or D + noble gas species admixtures) but it does not address how you would actually get the impurities into the plasma. Indeed, the required time scale and location at which impurities are inserted in the plasma by massive gas injection or pellets is a central issue in the acceptability of current designs for the ITER runaway mitigation system. If the impurity deposition profile would be very non-uniform, the results would be modified. The effect on the simulations here reported might be carried out once conclusive results are reached regarding the impurity penetration and deposition profile (as, for example, using the JOREK code [47]). Nevertheless, it can be expected that, if the impurity penetration into the plasma is not large enough, runaway mitigation in the central plasma region should be small and similar runaway currents to the worst cases here reported (long current quenches) would be obtained, i.e. ∼10 MA for the case of the hot-tail seeds with low t_0 and ∼4 MA for the tritium and Compton seeds as well as somewhat more peaked runaway current profiles would result which could lead to more MHD unstable runaway beams.

(c) The effect of the breakup of the magnetic surfaces during rapid thermal quenches [47–50] constitutes a central issue of the research on runaway electrons in ITER as the breakup of magnetic surfaces might spread the effect of the injected impurities for runaway mitigation and, on the other hand, might prevent the runaway electrons from reaching relativistic energies [50].

(d) Assessment of the impact of the stability boundaries ($l_{\mathrm{int}} - q_a$) on the mitigation scenario and magnetic energy conversion during the termination phase of the disruption. As discussed in section 3.1, the formation of peaked current density profiles during the current quench phase of the disruption typically yields MHD unstable plasmas. The implications for the termination and loss of the runaway beam should be the subject of future investigations such as the expected spatial and time location of the runaway losses, which is beyond the scope of this paper. To a certain extent, it can be assumed that the results reported in this work regarding the conversion of magnetic into runaway kinetic energy during disruption termination correspond to a worst case scenario as it has been considered that, when the termination phase starts, the peaking of the runaway current density profile does not change which, as it has been discussed in section 3.2, increases the amount of energy deposited on the runaway electrons. The excited MHD instabilities when the runaway beam crosses the stability boundaries could give rise to a redistribution of the current which might reduce the central peaking and, hence, the amount of energy that would be deposited on the runaways during current termination.

(e) In section 3.2, the conversion of magnetic into runaway kinetic energy during the termination phase of the disruption was discussed. Taking into the large uncertainties regarding the processes leading to the loss of the runaway current, a simplified approach has been used assuming that the runaway electrons are lost in single event with a characteristic loss time $\tau_{\mathrm{L}} \sim 0.1$–10 ms which has been shown to capture much of the physics underlying the termination of the runaway plasmas in several devices (JET, DIII-D and FTU) [6]. This approach has demonstrated to work reasonably well even when the runaway electrons are lost in a series of bursts if the estimate used for τ_{L} describes the whole duration of the runaway loss (including all the bursts) and not only a single event. However, to obtain more confident predictions for ITER demands a predictive capability regarding the runaway losses such as how such a characteristic loss time would scale for ITER or how the loss time depends on the electron energy (no dependence has been assumed in τ_{L}), which will be determined by the nature of the processes leading to the runaway losses, and which is beyond of the aim of this paper.

Acknowledgments

The authors wish to thank to S. Konovalov and V. Zogolev for discussions on the comparison of 0D and 1D models with DINA simulation results. This work was carried out with financial support from Direcció n General de Investigación, Científica y Técnica, Projects No.ENE2012-31753, ENE2015-66444-R (MINECO/FEDER, UE) and from the ITER Organization under contract IO/13/CT/430000875. ITER is the Nuclear Facility INB no. 174. This paper explores physics processes during the plasma operation of the tokamak when disruptions take place; nevertheless the nuclear operator is not constrained by the results of this paper. The views and opinions expressed herein do not necessarily reflect those of the ITER Organization. The authors would like to thank the referees for their constructive suggestions and criticisms which have contributed to improve the clarity and quality of the paper.

References

[1] Hender T.C. *et al* 2007 Progress in the ITER physics basis chapter 3: MHD stability, operational limits and disruptions *Nucl. Fusion* **47** S128
[2] Yoshino R. *et al* 1997 *Plasma Phys. Control. Fusion* **39** 313
[3] Putvinski S. *et al* 1997 *Plasma Phys. Control. Fusion* **39** B157
[4] Loarte A. *et al* 2011 *Nucl. Fusion* **51** 073004
[5] Hollmann E. *et al* 2013 *Nucl.Fusion* **53** 083004
[6] Martin-Solis J.R. *et al* 2014 *Nucl. Fusion* **54** 083027
[7] Martin-Solis J.R., Sanchez R. and Esposito B. 2000 *Phys. Plasmas* **7** 3369

[8] Bozhenkov S.A. *et al* 2008 *Plasma Phys. Control. Fusion* **50** 105007
[9] Martin-Solis J.R., Loarte A. and Lehnen M. 2015 *Phys. Plasmas* **22** 082503
[10] Gill R.D. *et al* 2002 *Nucl. Fusion* **42** 1039
[11] Eriksson L.-G. *et al* 2004 *Phys. Rev. Lett.* **92** 205004
[12] Smith H. *et al* 2006 *Phys. Plasmas* **13** 102502
[13] Helander P. 2007 *Phys. Plasmas* **14** 122102
[14] Aleynikova K., Huijsmans G.T.A. and Aleynikov P. 2016 *Plasma Phys. Rep.* **42** 486
[15] Martin-Solis J.R. *et al* 2006 *Phys. Rev. Lett.* **97** 165002
[16] Dreicer H. 1960 *Phys. Rev.* **117** 329
[17] Connor J.W. and Hastie R.J. 1975 *Nucl. Fusion* **15** 415
[18] Smith H. and Verwichte E. 2008 *Phys. Plasmas* **15** 072502
[19] Rosenbluth M.N. *et al* 1997 *Nucl. Fusion* **37** 1355
[20] Boozer A.H. 2015 *Phys. Plasmas* **22** 032504
[21] Aleynikov P. and Breizman B.N. 2015 *Phys. Rev. Lett.* **114** 155001
[22] Mosher D. 1975 *Phys. Fluids* **18** 846
[23] Martin-Solis J.R., Loarte A. and Lehnen M. 2015 *Phys. Plasmas* **22** 092512
[24] Parks P.B. *et al* 1999 *Phys. Plasmas* **6** 2523
[25] Kruskal M.D and Bernstein I.B. 1962 *PPPL Report* 174 MATT-Q-20
[26] Knoepfel H., Rosenbluth M.N. and Spong D.A. 1979 *Nucl. Fusion* **19** 785
[27] Igitkhanov Y.L. 2012 *Contrib. Plasma Phys.* **52** 460
[28] Smith H. *et al* 2009 *Plasma Phys. Control. Fusion* **51** 124008
[29] Feher T. *et al* 2011 *Plasma Phys. Control. Fusion* **53** 035014
[30] Loughlin M. and Polunovskiy E. 2016 private communication
[31] Iida H. *et al* 2004 Nuclear analysis report https://fusion.gat.com/iter/iter-fdr/final-report-sep-2001/Plant_Assembly_Documents_(PADs)/Nuc_Analysis_Report(NAR).pdf
[32] ITER Physics Expert Group on Confinement, Transport, ITER Physics Expert Group on Confinement Modelling, Database and ITER Physics Basis Editors 1999 *Nucl. Fusion* **39** 2175
[33] Klein O. and Nishina Y. 1929 *Z. Phys.* **19** 853
[34] Putvinski S. *et al* 2010 *Fusion Energy Proc. 23rd Int. Conf. (Daejeon, 2010)* (Vienna: IAEA) CD-ROM file ITR/1-6 (www-naweb.iaea.org/napc/physics/FEC/FEC2010/papers/itr 1-6.pdf)
[35] Sugihara M. *et al* 2007 *Nucl. Fusion* **47** 337
[36] Summers H.P. 1994 Atomic data and analysis structure Users Manual Report JET-IR 06, JET Joint undertaking, Abingdon
[37] Lukash V.E., Mineev A.B. and Morozov D.Kh. 2007 *Nucl. Fusion* **47** 1476
[38] Martin-Solis J.R. *et al* 2014 *Presented at 25th Int. Conf. on Fusion Energy (St. Petersburg, 2014)* TH/P3-43 (www-naweb.iaea.org/napc/physics/FEC/FEC2014/fec2014-preprints/143_THP343.pdf)
[39] Konovalov S. *et al* 2014 *Presented at 25th Int. Conf. on Fusion Energy (St. Petersburg, 2014)* TH/P3-31 (www-naweb.iaea.org/napc/physics/FEC/FEC2014/fec2014-preprints/561_THP331.pdf)
[40] Lukash V.E. *et al* 2013 Study of ITER plasma position control during disruptions with formation of runaway electrons *40th EPS Conf. on Plasma Physics (Helsinki, Finland)* p 5.167 (http://ocs.ciemat.es/EPS2013PAP/pdf/P5.167.pdf)
[41] Riccardo V. and Loarte A. 2005 *Nucl. Fusion* **45** 1427
[42] Wesson J.A. *et al* 1989 *Nucl. Fusion* **29** 641
[43] Aleynikova K.O. *et al* 2013 *Proc. 40th EPS Conf. on Plasma Physics (Espoo)* vol 37D (European Physical Society) O5.103 (http://ocs.ciemat.es/EPS2013PAP/pdf/O5.103.pdf)
[44] Aleynikov P. *et al* 2014 *Presented at 25th Int. Conf. on Fusion Energy (St. Petersburg, 2014)* TH/P3-38 (www-naweb.iaea.org/napc/physics/FEC/FEC2014/fec2014-preprints/319_THP338.pdf)
[45] Saint-Laurent F. 2010 *Proc. 23rd Int. Conf. on Fusion Energy (Daejeon, 2010)* (Vienna: IAEA) CD-ROM file EXS/P2-16 (www-naweb.iaea.org/napc/physics/FEC/FEC2010/papers/exs_p2-16.pdf)
[46] Lehnen M. *et al* 2015 *J. Nucl. Mater.* **39–48** 463
[47] Nardon E. *et al* 2017 *Plasma Phys. Control. Fusion* **59** 014006
[48] Izzo V.A. *et al* 2011 *Nucl. Fusion* **51** 063032
[49] Fil A. *et al* 2015 *Phys. Plasmas* **22** 062509
[50] Boozer A.H. *et al* 2016 *Phys. Plasmas* **23** 082514